Fall 2022

A Hybrid Experimental-Computational Study: Prediction of Flow Fields and Full-Field Pressure Distributions on Three-Tab Asphalt Roofing Shingles Subjected to Hurricane Velocity Winds

Troy A. Myers

A HYBRID EXPERIMENTAL-COMPUTATIONAL STUDY: PREDICTION OF FLOW FIELDS AND FULL-FIELD PRESSURE DISTRIBUTIONS ON THREE-TAB ASPHALT ROOFING SHINGLES SUBJECTED TO HURRICANE VELOCITY WINDS

by

Troy A. Myers

Bachelor of Science
University of South Carolina, 2020

Submitted in Partial Fulfillment of the Requirements

For the Degree of Master of Science in

Mechanical Engineering

College of Engineering and Computing

University of South Carolina

2022

Accepted by:

Michael A. Sutton, Director of Thesis

Fabio Matta, Reader

Cheryl L. Addy, Interim Vice Provost and Dean of the Graduate School

ACKNOWLEDGEMENTS

The support of the Department of Mechanical Engineering at the University of South Carolina was essential for the completion of this work and is gratefully acknowledged. The support of Mr. William Bradley and all members of the University of South Carolina Department of Mechanical Engineering Machine Shop in the development and manufacturing of the model roofing structure for wind loading is deeply appreciated. Finally, substantial funding provided by University of South Carolina Vice President for Finance Edward Walton via internal grant 15540 E250 for the development of our laboratory is gratefully acknowledged.

ABSTRACT

A novel hybrid experimental-computational study is performed to predict the flow fields and pressure distributions on the measured shapes of flexible, three-tab asphalt roofing shingles undergoing increasing uplift when exposed to hurricane velocity winds. StereoDIC analysis is performed to measure the transient full-field deformed shapes of full-size three-tab asphalt shingles when subjected to hurricane velocity winds for two hours. Steady state computational fluid dynamics (CFD) simulations of the shingled roof facsimile-plenum region representative of the experiments are successfully performed. The simulations are performed to predict wind loading of the uplifted shingle shapes by utilizing the measured full-field three-dimensional uplifted shapes of the roofing shingles at different time instances. Simulation predictions clearly show flow recirculation on both the front and top of the shingles, with the recirculation regions controlling the full-field uplifting pressure distribution. For low velocities, the predicted pressures from the CFD simulations are found to be in good agreement with prior measurements at corresponding locations where shingle uplift is ≤ 8.4 mm. For both low and high-speed flows, the model predictions indicate that high pressures are formed at the leading-edge upstream of the sealant layer, with the maximum pressure occurring along the leading-edge of the shingle near the tab cutouts. Under hurricane velocity winds, predictions indicate the leading-edge pressures are significantly higher than average values upstream of the sealant layer, increasing by ~ 55% prior to uplift and by ~26% during shingle uplift. The analysis indicates the maximum differential pressure, $\Delta P_{max} = 3.7kPa$, occurs at the leading-

edge for shingle uplift of 11.2 mm, with a slight decrease in pressure predicted for uplift > 11.2 mm. The combined experimental-computational studies provide a contemporary way to eliminate the difficulties associated with attachment of pressure sensors to flexible materials that can alter shingle response, while clearly delineating the physical processes of flow separation bubble formation and evolution that control asphalt shingle pressure loading and shingle uplift when exposed to hurricane velocity wind conditions.

TABLE OF CONTENTS

LIST OF FIGURES

LIST OF SYMBOLS

t	Time
s	Seconds
$\bar{B}$	Mean value of any variable, B
$P_{top}(x, y)$	Pressure on top of shingle
$P_{bottom}(x, y)$	Uplift pressure on bottom of shingle
$\Delta P(x, y)$	$P_{top} - P_{bottom}$, differential uplift pressure on shingle
ΔC_p	Uplift differential pressure coefficient
U_{ref}	Wind velocity approaching the roof
ρ	Air density
μ	Air dynamic viscosity
ν	Air kinematic viscosity
μ_t	Eddy-viscosity
$\mu t/\mu$	Turbulent viscosity ratio
I	Turbulence intensity

k	Turbulence kinetic energy
ω	Specific turbulence dissipation rate
y^+	Dimensionless distance from a wall
W_D	Width of Derickson's brass shingle tab
L_D	Length of Derickson's brass shingle tab
H_D	Thickness of Derickson's brass shingle tab
W_O	Width of the Owens Corning asphalt shingle tab
L_O	Length of the Owens Corning asphalt shingle tab
H_O	Thickness of the Owens Corning asphalt shingle tab
x, y	Spatial coordinates in plane of shingle
$w(x, y)$	Shingle uplift displacement field
$w(0, y)$	Leading edge uplift displacement
X_L	Normalized reattachment length
h	Step height
Re_h	Step Reynolds number
f_g	Wind gust frequency
K_c	Keulegan-Carpenter number

St	Strouhal number
T	Temperature
$\boldsymbol{t}$	Traction vector, components (t_x, t_y, t_z)

CHAPTER 1

INTRODUCTION

Asphalt roofing shingles are estimated to cover over eighty percent of residential homes in the United States, as the product's long history, ease of installation and affordable pricing make them an appealing option to both contractors and homeowners (ARMA 2014). Introduced in the late 19th century, asphalt shingles were individually cut and laid to resemble wooden or slate shingles. To cover a larger roof area in less time, individual shingles evolved into multi-tab shingles (Abraham 1918) to maintain the original shingled roof appearance.

Today, three-tab asphalt shingles are the most common shingle roofing system. Modern three-tab shingles typically are fastened to the wooden roof structure using roofing nails in a pattern of offset rows, with dimensions and general configuration shown in the schematic at top left of Figure 1.1. Also shown in Figure 1.1 is a span-wise strip of a thermally activated thermoplastic sealant. The sealant layer is located just behind the granulated upper surface region and row of roofing nails, and serves as the bond between individual overlapping shingles, forming a fully connected, contiguous roofing system. Since the sealant strip bond for each shingle is the only physical connection between shingles, it is the primary structural element resisting wind-induced uplift and separation of individual shingles.

Given the importance of shingle systems for the protection of a home, and the need to protect homeowners in areas where hurricanes and high wind conditions occur regularly, the wind resistance of roofing shingles has been a topic of research for several decades. The most significant early contributions were published by Peterka, Cermak, Derickson and Cochran, beginning with the development of a meteorological wind tunnel for near-earth characterization of wind flows (Cermak 1981) so that laboratory studies on structures, including roofs, could be performed in a manner that is consistent with the field environment. Early wind tunnel studies demonstrating wind effects on shingled roofs (Peterka and Cermak 1983) included flow-visualization studies that offered initial insight into the response of three-tab roofing shingles when subjected to modest winds. In their work, as depicted in Figure 1.2, the authors observed that uplift of a shingle caused wind flow changes that produced flow separation on the top surface near the leading-edge, commonly denoted as a "separation bubble". Flow reattachment was observed to occur at positions along the shingle that occurred further downstream as shingle uplift increased. Simultaneously, the authors characterized the uplifted shingle as a "bluff-body" in the air flow, resulting in increasing positive pressure[1] (+ sign region in Figure 1.2) on the bottom surface of the shingle up to the sealant layer location. In their studies, the combination of negative pressure (- sign region in Figure 1.2) in the separation bubble

[1] Consistent with standard terminology in fluid mechanics, pressure is defined to be positive when it provides compression on a surface and negative when it provides tension or uplift on a surface. Furthermore, differential pressure ΔP at any point on the bottom surface of the top shingle is defined to be $P_{top} - P_{bottom}$, where P_{top} is pressure at the point on the top surface with the same (x, y) coordinates as the corresponding point on the bottom surface.

on the top surface and positive pressure on the bottom surface results in a net uplifting pressure that increased uplift displacement in their studies.

Several years later, results were reported that expanded upon Peterka's work. In the first set of experiments (Cermak et al. 1991), results stemmed from additional experiments on scale model roofed buildings. This was followed by a series of wind tunnel studies on floor mounted roofing structures, performed with and without a flexible material attached to the front edge of the test stand to provide a smooth transition to the wind tunnel floor (Derickson et al. 1993). The experiments included air pressure measurements for an unsealed, specially fabricated brass shingle at several positions behind the shingle leading edge. Wind velocity measurements in their studies were obtained using a pitot tube located approximately 25 mm above and perpendicular to the roof surface and 50.8 mm behind the leading-edge. The investigators replaced asphalt shingles with nearly rigid brass shingle facsimiles so that they could attach pressure sensors without altering shingle response. In this way, they synthetically represent "uniform shingle uplift" through a hinge-like mechanism with a centrally located nut and bolt pair. The nut-bolt combination was used to accurately adjust the height of the leading-edge of the shingle relative to the roof surface. Upon subjecting the shimmed brass shingle simulants to relatively low velocity winds, Derickson recorded experimental pressure and near-shingle velocity measurements for several leading-edge heights. The pressure readings were then converted into a mean differential pressure coefficient, $\Delta\bar{C}_p$, defined by Equation 1.1 where $\Delta\bar{P}$ is the mean differential pressure, ρ is the density of the air and U_{ref} is the wind velocity approaching the roof.

$$\Delta \bar{C}_p = \frac{\Delta \bar{P}}{\frac{1}{2}\rho \bar{U}_{ref}^2} \quad (1.1)$$

Figure 1.3 shows the experimental results for $\Delta \bar{C}_p$ vs. uniform leading-edge uplift displacement for left, central and right areas of a mid-tab shingle (see Figure 1.1), with each area extending 32 mm behind the leading edge of their unsealed brass shingle facsimiles.

With consideration of building codes utilizing a gust factor approach, investigators (Peterka et al. 1997) proposed a quasi-steady wind uplift model to estimate the peak differential pressure that occurs on a single tab of a shingled roof due to incident winds. Their studies concluded with a final set of data obtained from wind tunnel experiments on scale model low-profile roofed buildings (Cochran et al. 1995). Based upon good agreement between a set of full-scale field experiments and their wind tunnel studies, their developments served as the foundation for standards such as ASTM D7158 (ASTM 2016). Since a majority of commercially available asphalt shingles have met D7158, they are designated Class H shingles and should be able to sustain wind loads of up to 190 mph without failure. Despite achieving this rating, such systems have tended to fail at wind speeds well below their design level, with significant variations in performance across brands (Insurance Institute for Business and Home Safety (IBHS) 2009).

Since previous studies, noted earlier, used rigid brass shingle simulants for the installation of sensors, thereby eliminating the direct installation of pressure sensors on asphalt shingles that would alter the shingle response and affect both uplift displacements and the measured pressure field, in our prior work (Rajan et al. 2020, Rajan et al. 2022)

the authors performed a series of experiments to directly measure the time-dependent, full-field uplift displacements of asphalt shingles with shingle sealant bonding that were subjected to hurricane velocity winds. The full-field deflections of several model three-tab shingle roofs were measured by using a non-contacting, stereovision-based measurement method, StereoDIC (Sutton 2009). The measurements (Rajan 2022) clearly show that a partially bonded sealant strip offers minimal resistance to shingle uplift, with uplift rapidly increasing and failure occurring within minutes. Furthermore, the experiments also reveal that a fully bonded sealant strip would undergo gradually increasing uplift without any sealant debonding, even when exposed to two hours of hurricane velocity winds.

Of particular interest in the full-field measurements was that the corners of the shingle near the tab cutouts incurred the highest levels of uplift which is consistent with other studies (Ghorbani et al. 2015, Rajan et al. 2022). These measurements indicate that the flow conditions in these regions are different. Since there was no evidence of sealant debonding at the end of the experiment, it can be inferred that the leading-edge near the tab cutout regions was incurring higher differential pressures as shingle uplift increased locally. Since direct measurement of the pressure difference across the flexible shingle is difficult and challenging, the author developed an alternative approach based on a combined experimental-computational approach to determine the full-field pressure differences across the entire area of each flexible shingle during hurricane velocity winds.

In the enclosed paper, the authors combine StereoDIC-based experimental measurements of full-field shingle deformations with computational fluid dynamics (CFD) simulations to predict the full-field differential pressure conditions that are driving

the complex, asphalt shingle uplift response when subjected to hurricane velocity winds. In Chapter 2 and Appendix A, the authors present a summary of the experimental procedure employed to measure the evolution of shingle uplift during two hours of exposure; a full description of the method and its application for shingle measurements is detailed in previous work (Rajan et al. 2022). In Chapter 3, the use of our new shingle shape measurements in the computational flow model is detailed. Chapter 4 presents both the mathematical formulae and the computational model. Chapter 5 is the longest section, providing detailed discussions of the computational findings along with comparisons to previously reported observations. Chapter 6 considers various application implications of our findings. Chapter 7 summarizes the results, highlighting improvements obtained in the current study.

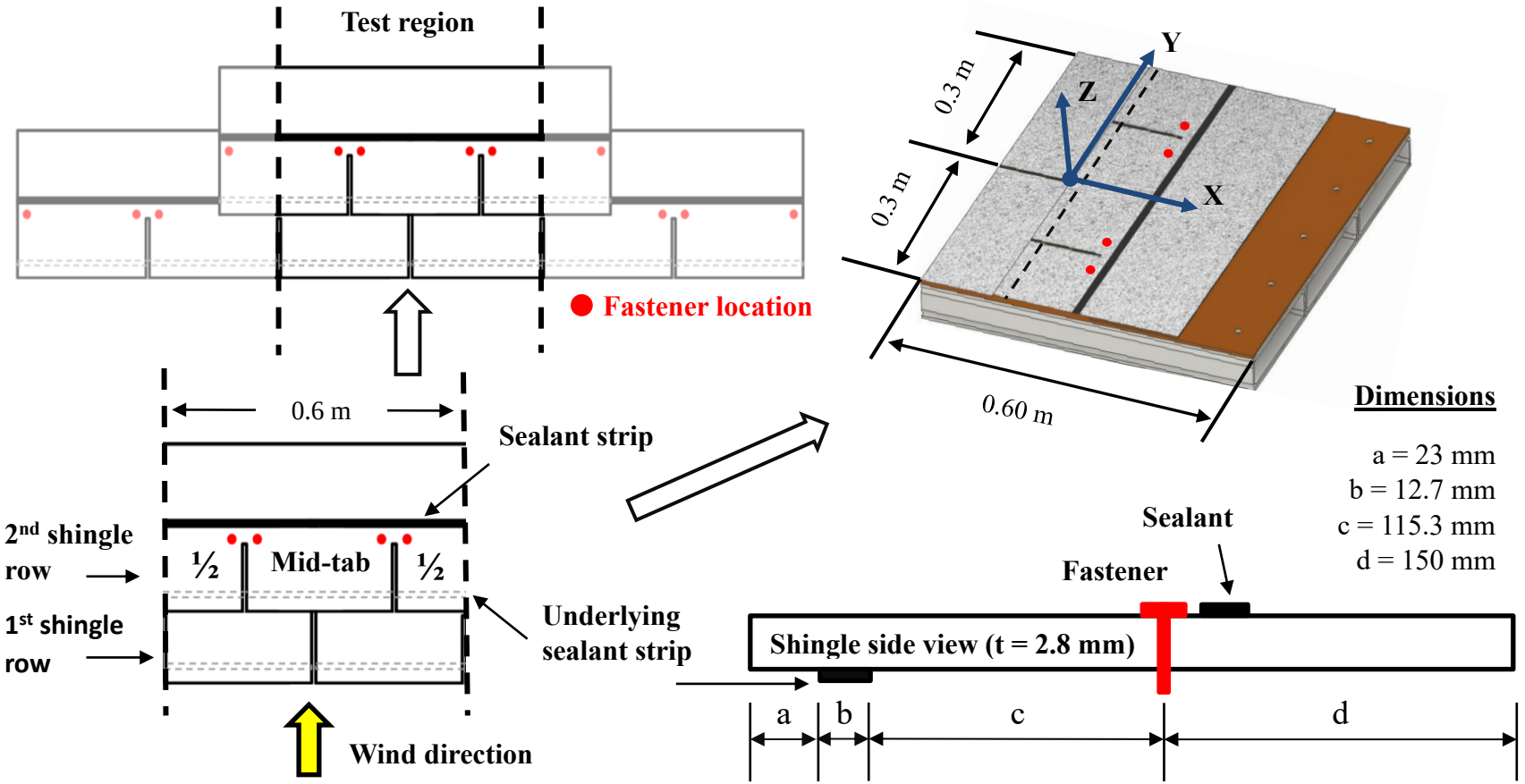

Figure 1.1 TOP: Three-tab asphalt shingle configuration on roof. BOTTOM LEFT: Schematic and overall dimensions for the shingled roof facsimile used in experimental and computational studies, with focus is on the mid-tab shingle in the 2nd row. RIGHT: Conceptualization of shingled roof facsimile with coordinate system and dimensions, including side view of shingle thickness. Shingles are nailed to 19.1 mm thick plywood base. Cartesian coordinate system (x, y, z) is centered in mid-tab and oriented along leading edge of mid-tab shingle with z-direction perpendicular to the panel.

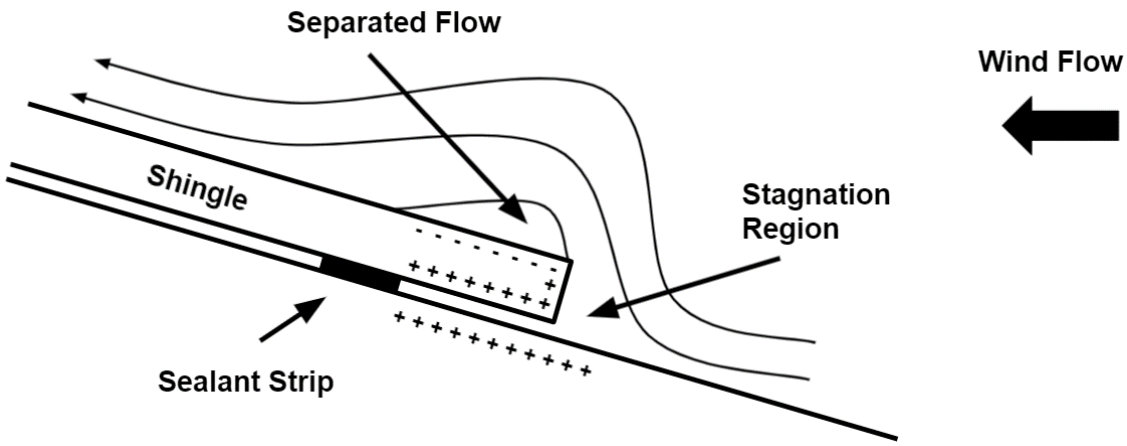

Figure 1.2 Shingle fluid mechanisms (Adapted from Peterka et al. 1997)

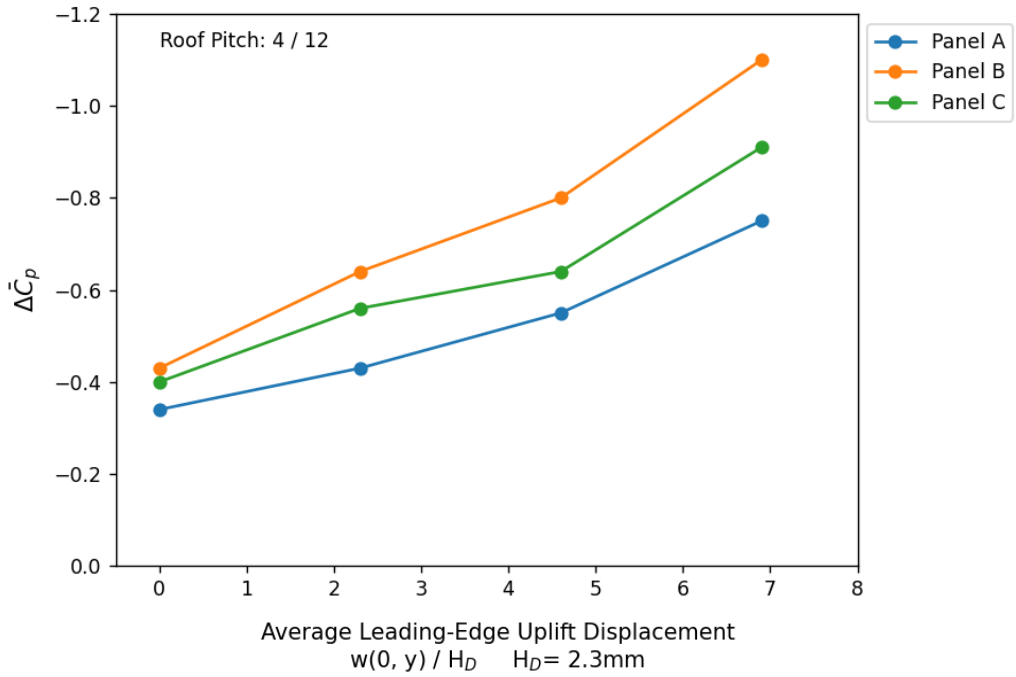

Figure 1.3 Experimental $\Delta\bar{C}_p$ vs. uniform leading-edge uplift displacement for rigid brass shingles subjected to low-speed winds. (Derickson 1993).

CHAPTER 2

EXPERIMENTAL PROCEDURE AND MEASURED THREE-DIMENSIONAL UPLIFT DISPLACEMENTS

Hurricane velocity wind loading experiments were conducted with Owens Corning Class H three-tab asphalt roofing shingles. In this work, a series of images were acquired at 1 Hz as 67.1 m/s hurricane velocity winds buffeted the shingled roof facsimile for two hours and twenty minutes (see Figure 1.1). Images were analyzed using StereoDIC (Sutton 2009, Rajan 2022) to obtain the experimentally observed shingle shapes and quantify the evolution of uplift displacements for the mid-tab shingle. Given the importance of this data for the computational modeling, details for the experiments, measurements, diagnostic procedures, and specimen fabrication are provided in the supplementary section in the form of Appendix A: Shape and Deformation Measurements Using StereoDIC for Full-size Three-Tab Shingles Subjected to Hurricane Velocity Winds.

The following observations of the as-measured, fully bonded shingle response during the hurricane velocity wind experiments are relevant to the CFD simulations.

- There were no visible vibrations or oscillation of the shingle at any time during the hurricane velocity wind experiments, an observation that is discussed further in Chapter 5.5.

- The evolution of shingle deformations during exposure to over two hours of hurricane velocity winds was temporally quite slow, without any jumps or shifts in the measured shapes. Shingle deformations and uplift progressed steadily throughout the wind loading process in a monotonically increasing manner.
- The sealant bond for the shingle mid-tab in the 2nd row of shingles remained intact throughout the experiment (for all 9600 s), with no visible bond separation. Post experiment examination confirmed that the entire length of the sealant remained attached without visible separations.

Given these observations, the authors selected six specific times during hurricane velocity winds to show the evolution of shingle deformations. Figure 2.1(a) – Figure2.1(f) present the measured full-field three-dimensional uplifted shingle shapes at $t = 0\ s$, $1500\ s$, $3000\ s$, $4800\ s$, $6600\ s$ and $8400\ s$, respectively, with the Figure 2.1 inset providing a close-up perspective of the complex, uplifted shingle shape in the leading-edge region. As shown, the evolution of shingle uplift is slightly spatially asymmetric, with larger uplift displacements, $w(x, y)$, near the tab cutouts on both sides of the shingle.

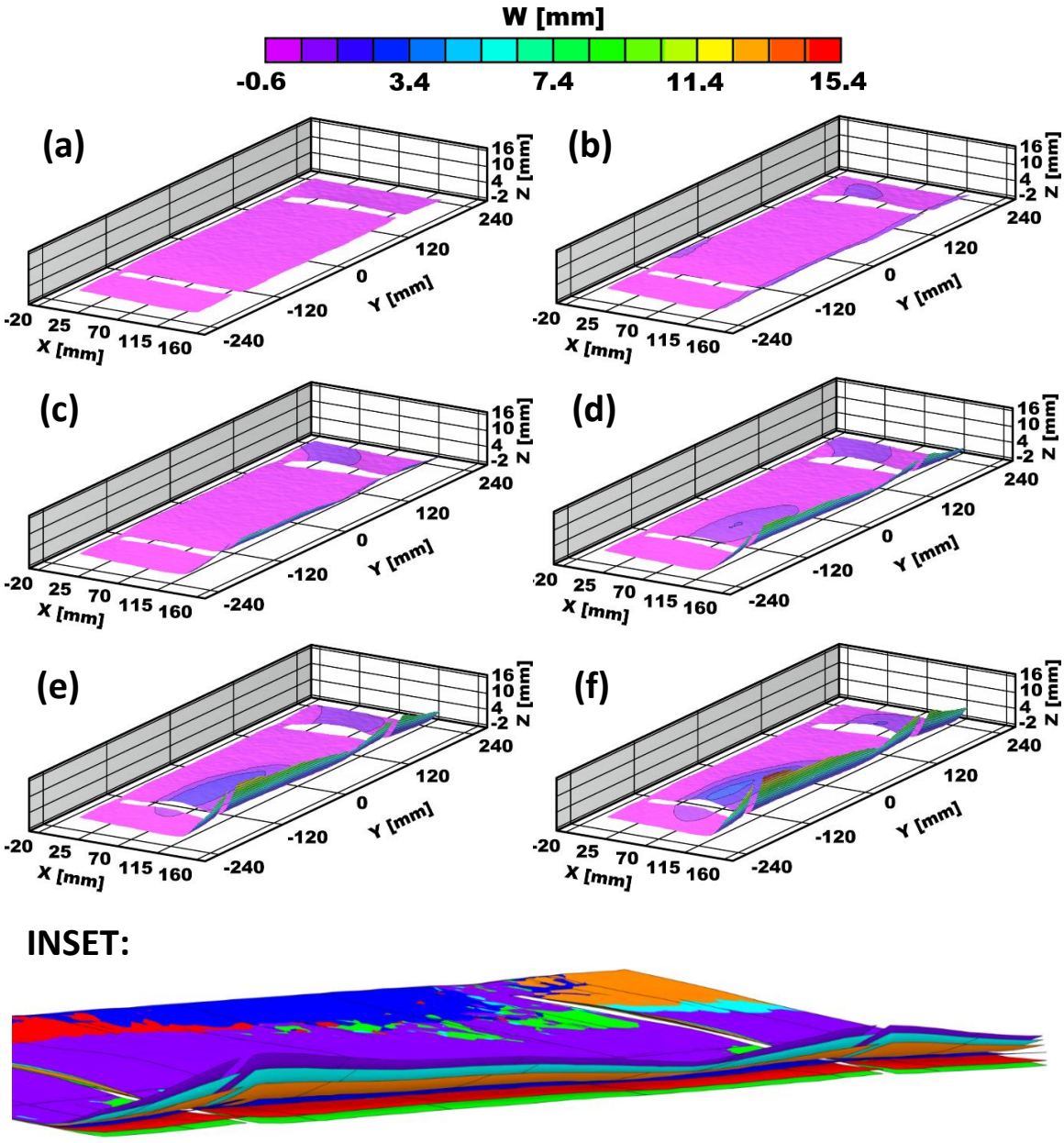

Figure 2.1 Deformed shapes of the 3-tab shingle at times (a) $t = 0\ s$, (b) $t = 1500\ s$, (c) $t = 3000\ s$, (d) $t = 4800\ s$, (e) $t = 6600\ s$ and (f) $t = 8400\ s$ during exposure to hurricane velocity winds. INSET: 3D graphical presentation of the measured shingles' shapes.

CHAPTER 3

OVERVIEW OF COMBINED EXPERIMENTAL-COMPUTAITONAL PROCEDURE FOR THE PREDICTION OF UPLIFT PRESSURE FIELDS FOR SHINGLES UNDERGOING WIND LOADING

To perform simulations and predict full-field uplift pressure distributions on the as-measured shingle shapes during hurricane wind loading, the authors integrated their full-field, three-dimensional surface displacement measurements for the three-tab shingle shown graphically in Figure 2.1 with the multi-physics CFD package, ANSYS Fluent. An overview of the process used in this study is shown in Figure 3.1, with details for each step outlined in the following paragraphs.

In the first phase, the full-field three-dimensional position measurements (x_i, y_i, z_i) are obtained at 33,670 points on the shingle roof facsimile at each time of interest using StereoDIC analysis software, VIC-3D (Correlated Solutions Incorporated). Spacing between data points for the 'point cloud of data' ranges from 1.2 mm to 1.4 mm at each time, t. Since shingle surface measurements are obtained in the deformed configuration, the shingle already has undergone wind-induced deformation. The data set is exported from VIC-3D in a .csv file format for further processing. In the second phase, the VIC-3D data file is imported into MATLAB and fitted with a 'v4' biharmonic spline

function[2]. After interpolation, 65,208 points are obtained with ~1 mm spacing between data points in the x-y plane[3]. In the third phase, the point cloud of data is imported into the software PTC Creo Parametric. The data is used to construct a triangular surface representation which is exported into a .STL file format. In the fourth phase, the .STL file is imported into ANSYS SpaceClaim, Within ANSYS, the "skin surface tool" converts the facet data into a boundary representation (B-Rep) by defining spline functions to interpolate the faceted data[4]. The authors' determined that it is best to divide the shingle region into several adjoining sections for import to the skin surface tool to ensure accurate surface reconstruction; all sections are automatically stitched together to create the entire shingle surface. As part of their studies, the authors showed that the default value of 50 points is sufficient to obtain high accuracy in each spline fit; the maximum deviation of the spline fit from the facet data for the entire shingle area is 0.05mm. In the fifth and final phase, the 'skin surface' representation is extruded to form a three-dimensional continuous structure with a thickness of 2.8 mm, which is the original thickness of the shingle (see Figure 1.1). The continuous structure is then manually edited to remove the shingle cutout regions, forming the complete *"½ tab - mid-tab - ½ tab"*

[2] The v4 biharmonic spline interpolation function in MATLAB is a linear combination of Green's functions centered at each data point. The amplitudes of the Green's functions are found by solving a linear system of equations, with the interpolation function passing directly through the measured z value for each data location (x, y).

[3] Though not used in our fluid-structure interaction studies, the data on both sides of the tab cutouts is used to fit a fictitious function to the virtual tab region to obtain a continuous function throughout the rectangular measurement region. Without prior interpolation to construct a continuous function, the 'skin surface tool' in the next phase attempts to interpolate the data in the missing regions, reducing the accuracy of the measurements in the nearby regions.

[4] A total of 50 control points per line are used to obtain a Non-Uniform Rational B-Spline (NURBS) fit to the triangular facet representation.

shingled roof shape at times $t = 0\ s$, $1500\ s$, $3000\ s$, $4800\ s$, $6600\ s$ and $8400\ s$ (see Figure 2.1).

After constructing the complete shingle portion, a sealant strip is added to the shingle using ANSYS. Assuming no debonding has occurred during wind loading, the sealant strip is placed between the upper and lower shingles, while enforcing displacement continuity at all contact points. At time $t = 0\ s$, the average sealant thickness after bonding is approximately 0.28 mm and the sealant width is 12.7 mm. Since the upper shingle undergoes uplift during wind loading and the lower shingle is undeformed, the bonded sealant layer is deformed to maintain bonding and complete the continuous shingle structure model. In this work, the sealant layer is constructed as a 12.7 mm wide layer with (a) an upper surface that corresponds with the lower surface of the top shingle and (b) a lower surface that is the upper surface of the bottom shingle[5]. Using this approach, a sealant layer is defined at each time, t, and then merged within ANSYS to construct a continuous shingle-sealant-mounting structure system for simulations. The combination of reconstructed, deformed shingle shapes with sealant layer bonded to the underlying support stand configuration are used in CFD simulations described in the following section to predict the flow and pressure fields during two hours of exposure to high-speed winds.

[5] The bottom surface of the shingle was not perfectly flat at the sealant location, especially after deformation. Though the minimum sealant thickness is set at 0.28 mm, to be consistent with measurements, the sealant model thickness will be slightly higher at some points along the shingle to maintain full bonding between sealant and upper shingle.

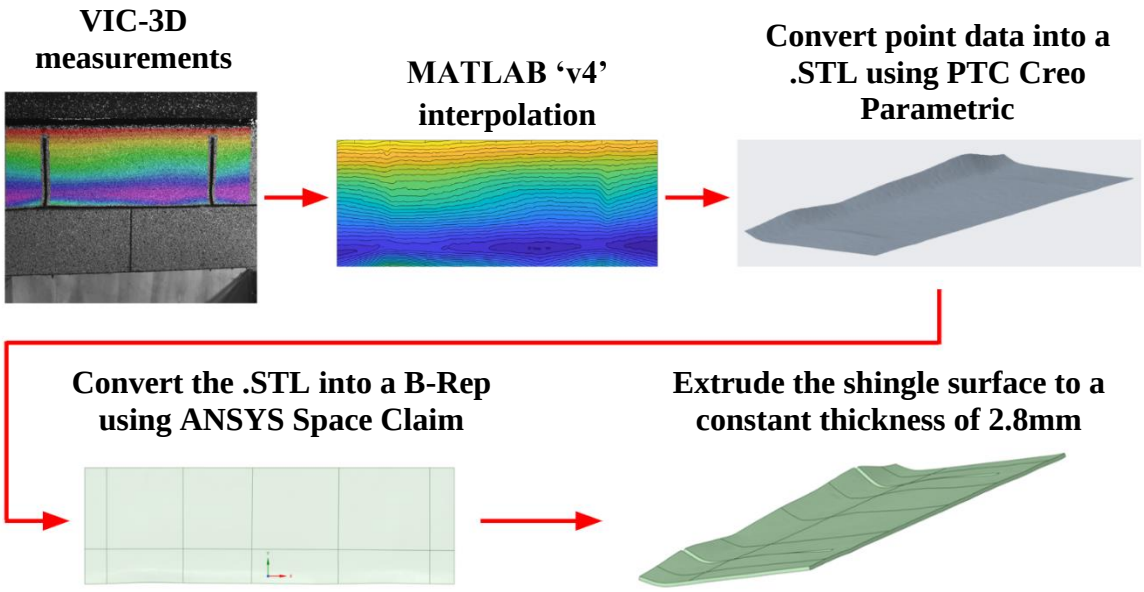

Figure 3.1 Schematic of the deformed shingle reconstruction process using StereoDIC measurements.

CHAPTER 4

MATHEMATICAL MODELING

To resolve the flow field, the steady state mass and momentum conservation defined in Equation 4.1 and 4.2, respectively, are solved simultaneously where p is static pressure and $\bar{\bar{\tau}}$ is the viscous stress tensor expressed as $\bar{\bar{\tau}} = \mu[(\nabla\vec{v} + \nabla\vec{v}^T) - \frac{2}{3}\nabla \cdot \vec{v}I]$.

$$\nabla \cdot (\rho\vec{v}) = 0 \tag{4.1}$$

$$\nabla \cdot (\rho\vec{v}\vec{v}) = -\nabla \mathrm{p} + \nabla \cdot (\bar{\bar{\tau}}) \tag{4.2}$$

A generalized $k - \omega$ (GEKO) turbulence formulation is utilized to model the turbulence effects where the turbulent kinetic energy and dissipation rate is modeled. The GEKO model is a two-equation model developed by ANSYS that is tunable through six parameters designated C_{CORNER}, C_{CURV}, C_{SEP}, C_{NW}, C_{MIX}, and C_{JET} (Mentor et al, 2020). The turbulence kinetic energy, k, is obtained from Equation 4.3 where $P_k = -\tau_{ij}\frac{\partial u_i}{\partial x_j}$, μ_t is the eddy-viscosity, and C_μ, σ_k are constants. The specific turbulence dissipation rate, ω, is obtained from Equation 4.4 where $CD = \frac{2}{\sigma_\omega}\frac{1}{\omega}\frac{\partial k}{\partial x_j}\frac{\partial \omega}{\partial x_j}$.

$$\frac{\partial(\rho u_j k)}{\partial x_j} = P_k - C_\mu \rho k\omega + \frac{\partial}{\partial x_j}[(\mu + \frac{\mu_t}{\sigma_k})\frac{\partial k}{\partial x_j}] \tag{4.3}$$

$$\frac{\partial(\rho u_j \omega)}{\partial x_j} = C_{\omega 1}F_1\frac{\omega}{k}P_k - C_{\omega 2}F_1\rho\omega^2 + \rho F_3 CD + \frac{\partial}{\partial x_j}[(\mu + \frac{\mu_t}{\sigma_\omega})\frac{\partial \omega}{\partial x_j}] \tag{4.4}$$

In its default configuration, the model closely resembles the commonly used $k-\omega$ shear stress transport (SST) model using four of the six free coefficients defined as $C_{SEP} = 1.75$, $C_{NW} = 0.5$, $C_{MIX} = 0.35 sign(C_{SEP}-1)\sqrt{|C_{SEP}-1|} = 0.23$ and $C_{JET} = 0.9$. An advantage of the GEKO model is its use of a blending function to combine aspects of the $k-\omega$ model in the near-wall region with a $k-\varepsilon$ model further away from the surface. Details regarding the process used within ANSYS/Fluent to determine the constants $C_{\omega 1}$, $C_{\omega 2}$, σ_{ω} and the functions F_1, F_2, F_3 are not readily available.

4.1 COMPUTATIONAL DOMAIN

Once the measured shingle geometry is converted into a structural model using the procedures described in Chapter 3, a 3D domain with roof facsimile is constructed for CFD simulations. Figure 4.1 shows a perspective view of the semi-spherical fluid domain used in this study. The spherical portion of the domain has an outer radius of 8.00 m with a no-slip boundary along the vertical bisecting plane, while also containing the wind tunnel system. The fluid domain-shingled roof model combination is constructed to represent the actual experimental configuration, with the shingled roofing section (see Figure 1.1) placed at the exit of the wind tunnel within the fluid domain and rotated upwards by 10° degrees. A side-view schematic of the wind tunnel with the shingled roofing section located just outside the outlet is shown in Figure A.2 in Appendix A.

Based upon our prior measurements (Rajan et al. 2020, Rajan et al. 2022), the lower shingle, plywood sheet and steel support structure shown in Figure A.2 did not incur measurable displacements or strains. Thus, all three are modeled as rigid, undeformed components throughout the wind loading process. Secondly, the upper

shingle was attached to the plywood sheet by screws to minimize local damage during shingle installation. Thus, consistent with the measured shingle shapes shown in Figure 2.1, the attachment area on the back of the shingle has displacements ≤ 1 mm throughout the wind loading process, and these deformed positions are incorporated in the model. Thirdly, neither visual observations nor StereoDIC measurements during hurricane velocity wind exposure showed any shingle vibrations. Thus, in this study the measured deformed shingle position is considered to be an instantaneous, non-deforming bluff body for analysis purposes.

Since (a) the wind tunnel used in these studies is not a meteorological system (Cermak 1981), (b) the shingled roof facsimile is placed just outside the wind tunnel exit and (c) the mean wind velocity is the only measured flow parameter, a series of 2D flow simulations were performed to characterize the as-supplied flow field that is incident on the shingled roof facsimile, comparing the predicted exit velocity profile to a fully developed velocity profile. Results from these simulations are given in Appendix B: Computational Characterization of Flow Conditions Incident on Shingled Roof Facsimile. In brief, results in Appendix B show that (a) turbulence intensity variations in the range $0.05 \leq I \leq 0.20$ and viscosity ratio variations in the range $10 \leq \mu t / \mu \leq 20$ have negligible impact on the CFD predictions, with the former range bounding the observed range seen in a previous set of experimental shingle studies (Cermak et al 1991)[6], (b) the exit velocity profile for the experimental wind tunnel with shingled roof facsimile in Figure A.2 is predicted to have much higher velocities near the shingled roof

[6] Based on findings in (a), the authors selected $I = 0.05$ and $\mu t/\mu = 10$ for all three-dimensional computational models.

surface and steeper velocity gradients than a fully developed velocity profile and (c) for an initially flat shingled roof facsimile, the exit velocity profile for the experimental wind tunnel is predicted to have higher uplift pressures than would be expected for a fully-developed profile.

4.2 CFD MESH AND MODELING DETAILS

A refined mesh structure for the shingle-sealant region containing octree hexahedral elements connected to layered poly-prisms within the boundary layer through a mesh of transitional polyhedral elements is constructed. A zoomed side-view of the mesh structure in the critical region near the sealant is shown in Figure 4.1. For the GEKO turbulence model, a near-wall meshing approach (ANSYS Fluent 2017) is implemented, with fifteen poly-prism element layers forming the boundary layer. The mesh structure has a maximum first cell height of 8.0 μm placed within the viscous sublayer. The constructed mesh maintained a y^+ value of $y^+ \approx 1.0$ and maximum element skewness is limited to 0.90 to minimize the possibility of numerical instability.

The governing equations are solved in three dimensions following the finite volume discretization approach. A pressure-based incompressible flow solution method is adopted and the pressure correction equation is discretized via the PRESTO methodology. A QUICK (Quadratic Upstream Interpolation for Convective Kinematics) scheme is used to discretize the flux terms in the momentum, turbulent kinetic energy and dissipation. At the inlet, the turbulent intensity and viscosity ratio were prescribed to be 5% and 10, respectively. To confirm a converged solution, the discretized set of equations are iterated until a residual level $\leq 10^{-3}$ is achieved. In addition, the convergence of physical quantities such as the lift and drag coefficient of the shingle are

considered during the assessment of solution convergence. To obtain a grid independent solution, the mesh was systematically refined. Grid independency was achieved for a total mesh size of ~4.6 million cells.

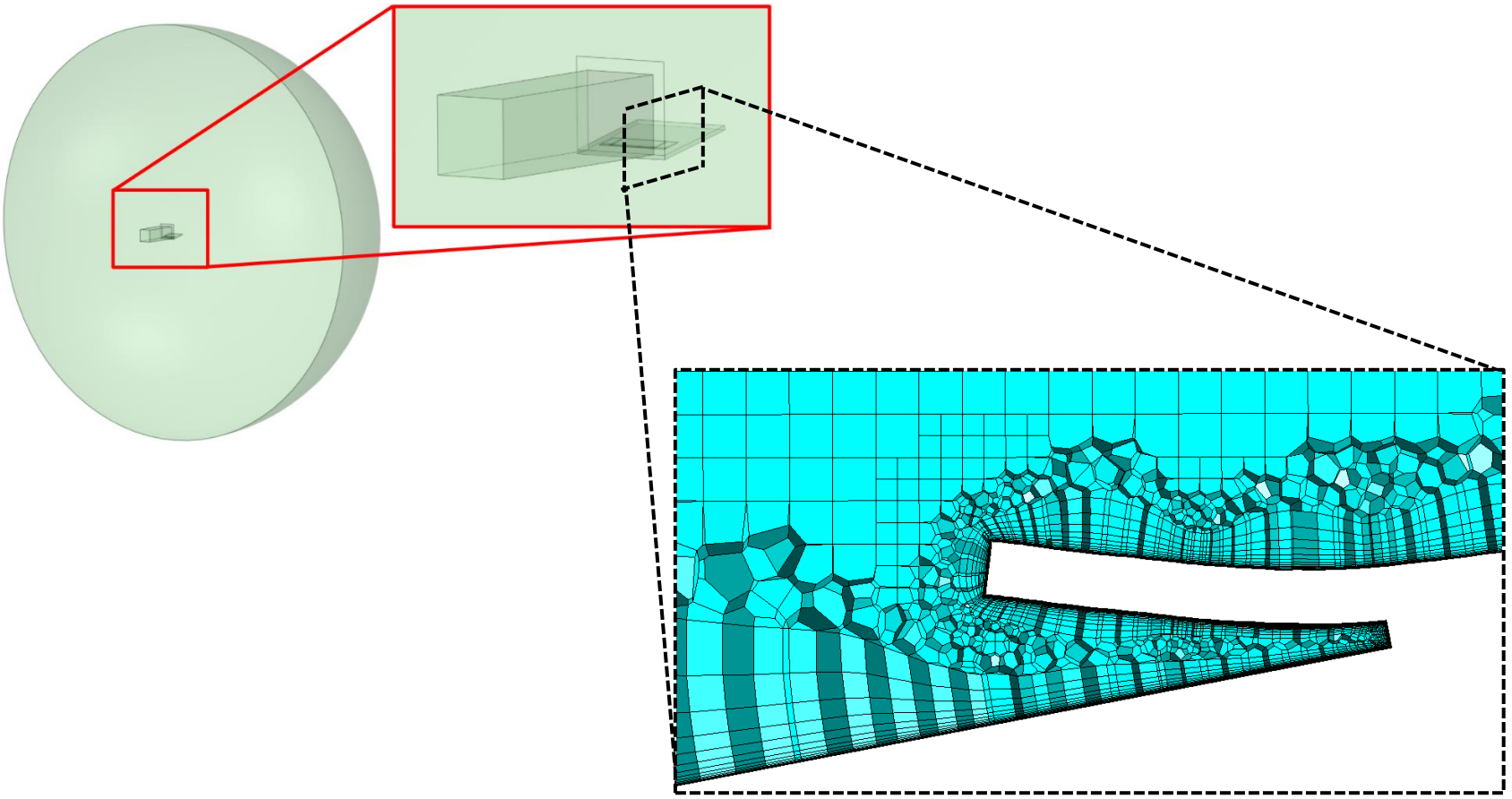

Figure 4.1 Perspective schematic of semi-spherical fluid domain, with radius $R = 8.00\ m$. Fluid medium is air under standard conditions. INSET: Side view of poly-hexcore meshing of the fluid domain in the leading-edge and sealant region for one of the six shingle uplift shapes.

CHAPTER 5

COMPUTATIONAL RESULTS

5.1 NOMINALLY FLAT SHINGLES: FLOW AND PRESSURE FIELD PREDICTIONS AND RELATIONSHIP TO PREVIOUS WORK

Shingle-sealant-structure simulations are performed for the nominally flat shingle-sealant-mount system rotated upwards by 10^o, as shown schematically in Figure A.2. In these simulations, the upper mid-tab shingle is attached to the substrate at both the sealant location and at the downstream attachment locations. To reflect the presence of many small air gaps between the upper and lower shingle due to extensive granulation of the lower substrate (shingle) surface, a small gap is inserted between the substrate and the shingle bottom surface for the CFD simulations. For an upstream inlet velocity of 67.1 m/s, the predicted equally spaced streamlines are shown in Figure 5.1. The streamline pattern shows several important features during the wind-loading process.

The first feature occurs at the low-profile front surface of the shingle, which acts as a small flow-field obstruction forming a localized separation bubble that is hereafter designated the “front-surface separation bubble”. As flow passes over the top edge of the shingle’s front surface, a second separation bubble is formed, designated hereafter as the “leading-edge separation bubble”. The leading-edge separation bubble extends downstream before reattaching to the shingle surface. These results are qualitatively

consistent with flow fields observed by previous investigators (Peterka and Cermak 1985). Careful inspection of the flow field near the leading edge of the shingle in Figure 5.1 shows the presence of increasing flow velocity with vertical position across the shingle thickness. The predicted pressure field for the flat shingle is also shown in Figure 5.1. The front edge velocity gradient creates variable pressure across the shingle thickness, with increasing pressure across the shingle thickness applying a clockwise moment. Combining this moment with uplifting pressure due to lower pressure on the top surface and higher pressure on the underside, these conditions tend to uplift the front edge of the shingle into the flow, resulting in the evolution of shingle shapes shown in Figure 2.1.

5.2 UPLIFTED SHINGLES: FLOW AND PRESSURE FIELD PREDICTIONS FOR THE MEASURED SHAPES

The predicted flow and pressure fields in z-x plane along centerline of specimen ($y = 0$) for the measured, uplifted shingle shapes at $t = 1500\ s$ and $3000\ s$ are shown in Figure 5.2(a) and Figure 5.2(b), respectively. The flow and pressure field at other time instances are visually similar and therefore are not shown here. As shown in Figure 5.2(a) and Figure 5.2(b), simulations indicate that uplifted shingle shapes form two separation bubbles, including an expanded front surface separation bubble due to the increasing frontal area as the shingle uplifts and a leading-edge separation bubble. Comparison of the flow fields in Figure 5.2(a) and Figure 5.2(b) shows that increasing uplift (i.e. an increasing angle of attack) results in an increase in the size and extent of separation bubbles. For small amounts of uplift, the leading-edge separation bubble reattaches to the upper shingle surface, with reattachment length increasing with uplift. For larger uplifts,

the leading-edge separation bubble extends beyond the shingle. Streamline predictions shown in Figure 5.2(a) are qualitatively consistent with previous computational work (Yang et al. 2010) for near-ground wing structures subjected to wind loading.

5.3 COMPARISON OF CFD PRESSURE PREDICTIONS TO PREVIOUS EXPERIMENTAL RESULTS

The modeling framework also is employed to simulate the pressure distribution of reduced wind velocity experiments conducted previously (Derickson et al. 1993) for comparison to their measurements. As shown in Figure 5.3, Derickson and his colleagues installed nine pressure taps positioned on a rigid brass shingle along a line located a distance W from the leading-edge. The authors reported the average of the three pressure sensors in each $L/3$ by $2W$ area behind the leading-edge (denoted by A, B and C in Figure 5.3) for uplift displacements of 0 mm, 2.8 mm, 5.6 mm and 8.4 mm. Their average pressure measurements in areas A, B and C were acquired during exposure to relatively low-speed winds, on the order of 10 m/s (see Figure 1.3). To compare simulation predictions to Derickson's pressure measurements[7], the measured shingle shapes at times $t = 0\ s$, $1500\ s$, $3000\ s$ and $4800\ s$ (see Figure 2.1) are subjected to 10 m/s winds[8]. The predicted pressures on the top and bottom of each shingle shape are averaged over sections A, B and C (Figure 5.3). In addition, the corresponding uplift values at times $t = 0\ s$, $1500\ s$, $3000\ s$, $4800\ s$ obtained using our StereoDIC measurements are averaged along the entire leading-edge length spanned by sections A, B and C. Figure 5.4 shows

[7] Pressure measurement locations in ASTM D7158 (2016) are along this line but are located on the underlying roof structure.

[8] The shingle shapes at these times were selected since the average uplifts for these times spanned the range of uplifts used in the brass shingle studies.

the average $\Delta\bar{C}_p$ in the areas A, B and C versus the average leading-edge uplift displacement for (a) Derickson's data shown as symbols for the average in each area, (b) our CFD predictions using the measured three-dimensional shingle shapes for 10 m/s winds at the times when uplift was closest to those in Derickson's study and (c) our CFD predictions using the measured three-dimensional shingle shapes for hurricane velocity winds with speed of 67.1 m/s at the same times. For low-speed winds, both the CFD predictions for as-measured asphalt shingle shapes and experimental measurements for a flat shingle (no uplift) have similar trends, with $\Delta\bar{C}_p$ increasing with leading edge uplift. Though the general trends agree, there are also differences.

First, as shown in Figure 5.4, the CFD predictions using the as-measured asphalt shingle shapes are nearly the same in all three sections, whereas previous experimental measurements show substantial differences between sections. Since the CFD simulations used the actual, non-uniformly deformed and uplifted shingle shapes, the geometry introduced local flow conditions that tend to equilibrate the average pressures in sections A, B, C, resulting in similar $\Delta\bar{C}_p$ values across the entire shingle span. Conversely, the rigid planar brass shingle configuration used in the experimental studies retained its planar geometry for each uplift, resulting in conditions that induced asymmetric uplift pressures across the width of the shingle.

Secondly, the averaged CFD pressure data for Sections A, B and C in Figure 5.4 appear to be slightly concave downwards as uplift increases, whereas previous experimental pressure measurements versus shimmed uplift over the limited range of uplift appeared to be slightly convex upwards. In this regard, a significant contributing

factor towards the differences between the experimental and computational predictions for $\Delta\bar{C}_p$ values may be the exact location of the mean roof velocity measurements, as discussed in the following paragraph. In Derickson's experiments, the velocity measurements were acquired at a fixed location for all levels of uplift, approximately 25 mm above the initial roof surface and 50.8 mm behind the leading-edge of the brass shingle. For the simulation results shown in Figure 5.5, the same approach was taken using a line sample placed in the same position behind the leading-edge, extending 23 to 28 mm above the roof surface for an average position of 25 mm. If the velocity measurement position was slightly lower, ranging between 20mm and 25mm, the predicted velocities near the shingle will decrease with increasing uplift due to the presence of a steep vertical velocity gradient as flow passes over the leading edge. Depicting new velocity measurement location(s) shown as solid black lines that are closer to the shingle in Figure 5.5, an updated comparison of CFD predictions to the original data is shown in Figure 5.6. Results show that for velocity measurement locations in the range 20 to 25 mm above the original shingle, $\Delta\bar{C}_p$ predictions will increase with uplift since the upper surface velocity predictions will decrease with larger uplift, creating a convex upward trend that is qualitatively like the experimental data.

Thirdly, the distinct differences in the experimental setups (e.g. central bolt and nut pair used to incrementally raise the leading-edge shingle height, no shingle sealant, rigid shingle, wind tunnel configuration, specimen positioning) may have an effect on the measurements but have not been addressed in the simulations which utilize the as-measured shingle shapes. For hurricane velocity winds of 67.1 m/s, the predicted average pressures in Sections A, B and C are also shown in Figure 5.4, again showing span-wise

symmetry in the $\Delta\bar{C}_p$,with the $\Delta\bar{C}_p$ values predicted to be much higher for hurricane velocity winds.

Another difference between previous low-speed wind studies and the current experimental-computational investigation is related to the effect of wind speed on $\Delta\bar{C}_p$. Considering only the results for 0 mm uplift (flat shingle), previous $\Delta\bar{C}_p$ results (Cermak et al. 1983) for wind velocities in the range of 8.94 m/s to 11.18 m/s indicate a nominal independence of $\Delta\bar{C}_p$ relative to the mean Reynolds number. However, for the same planar shingle geometry our computational predictions for 10 m/s and 67.1 m/s winds shown in Figure 5.4 indicate that similitude does not exist for 10 m/s and 67.1 m/s velocity flows, with the $\Delta\bar{C}_p$ values increasing approximately 50%.

As to the reason for increasing $\Delta\bar{C}_p$ with flow velocity, the work of Sherry et al. (2009) is relevant. In their studies, the authors noted that expansion of the leading-edge separation bubble with velocity is characteristic of forward-facing steps. Their studies show that the normalized reattachment length, $X_L = x/h$, where x is physical distance perpendicular to the leading-edge and h is the frontal step height, is sensitive to many flow parameters including (a) the ratio δ/h, where δ is the upstream boundary layer thickness and (b) the step Reynolds number, $Re_h = \frac{U_\infty h}{\nu}$, where U_∞ is the incoming free-stream velocity and ν is the kinematic viscosity of the working fluid. They identified two regimes; one when $Re_h < 8500$ and $X_L = X_L(Re_h)$ and a second regime when $Re_h > 8500$ and X_L is weakly dependent on Re_h and independent of δ/h. In our study, the physical reason for this regime shift is shown to be a direct result of changes in the front-surface and leading-edge separation bubbles with Re_h. For the specific wind tunnel-

specimen geometry employed in this study, additional CFD simulations were performed for the flat shingle geometry with 10 m/s and 67.1 m/s winds. Using the shingle thickness of 2.8mm as the step height for the 10 m/s case, $\delta/h = 12.5$ and $Re_h = 1940$. Upon increasing the inlet velocity to 67 m/s, $\delta/h = 6.57$ and $Re_h = 12{,}885$. In addition, along the center of the shingle, the reattachment length, X_L, for a flat shingle increased from 11.8 mm for 10 m/s winds to 14.6 mm for 67.1 m/s winds, a 24% increase[9]. Noting that the location where pressure predictions are obtained, $W_O = 11.5\ mm$ from the leading-edge (see Figure 5.3), is in the bubble reattachment zone for low velocity flow, this results in lower uplifting pressure predictions on the top surface and hence a reduced $\Delta\bar{C}_p$. Conversely, for hurricane velocity winds in the range of 67 m/s, the same pressure prediction location for a flat shingle is well within the larger leading-edge separation bubble, resulting in much higher uplift pressure predictions and hence a larger $\Delta\bar{C}_p$ prediction. For all non-zero levels of uplift, the pressure measurement location is well within the leading-edge separation bubble for hurricane velocity winds of 67.1 m/s, resulting in larger $\Delta\bar{C}_p$ predictions relative to those at lower velocities. Thus, expansion of the shingle separation bubbles with increasing wind velocity is the physical phenomenon associated with dependence of $\Delta\bar{C}_p$ on the step Reynolds number.

[9] Though the numerical values of the shingle reattachment lengths do not fall within the range of data collected by Sherry et al. in their experimental setups, the trend of increasing reattachment length with decreasing δ/h and increasing Re_h is consistent with their work.

5.4 PREDICTED PRESSURE FIELDS FOR THE ENTIRE SHINGLED REGION

Since our CFD simulations provide full three-dimensional pressure data, the simulations can be used to visualize the entire pressure field. Figure 5.7 shows the pressure fields on the top and bottom surfaces of the shingled roof facsimile, as well as the shear stress field on the top surface at times $t = 1500$ s, 4800 s and 8400 s for a wind speed of 67.1m/s. Inspection of the full-field pressure predictions in Figure 5.7 shows two specific features. First, consistent with various previous studies, the predictions show the shingle area between the leading-edge and the sealant strip experiences the largest direct uplift pressure on the bottom surface, with maxima occurring near both the leading-edge and along the vertical tab cutouts shown in Figure 1.1. The predicted pressure at the intersection of the leading-edge and the tab cutout is up to 30% higher than the average on the area ahead of the sealant strip. Secondly, as shown in Figure 5.7, the pressure fields behind the sealant strip on both the top and bottom surface decrease by more than 1 kPa, resulting in much lower uplift pressures on the shingle in this region.

5.5 PRESSURE PREDICTIONS FOR THE LEADING-EDGE REGION USING FULL FIELD RESULTS

The full-field pressure predictions during wind loading, can be used to show more localized discrete pressure predictions in the region upstream of the sealant layer. As shown in Figure 5.3, sections A, B and C and A_{LE}, B_{LE} and C_{LE} along the leading-edge shown in Figure 5.3 are individually split into two equal parts, designated by L and R for each section. Figure 5.8(a) and Figure 5.8(b) show the localized mean differential pressure results, $\Delta\bar{P}$, versus the average leading edge uplift displacement in sections A_{LE}^{L},

A_{LE}^{R}, …., C_{LE}^{R} (a) at $W_O = 11.5\ mm$ behind the leading-edge and (b) at the leading-edge, $x = 0$, for times $t = 0\ s$, $1500\ s$, $3000\ s$, $4800\ s$, $6600\ s$ and $8400\ s$. The percent difference between the two sets of data is shown in Figure 5.8(c).

As shown in Figure 5.8(a), at $x = 11.5\ mm$ behind the leading-edge, tight clustering of all trend lines indicates that $\Delta\bar{P}$ is relatively uniform across the asphalt shingle span at this distance behind the leading edge. As noted previously, our predictions at time $t = 0\ s$ indicate an initially flat shingle exposed to winds will immediately experience uplift pressure due to a combination of uplift pressure on top of the shingle and the upward pressures on the bottom surface of the shingle due to infiltration of high-speed air into the front gap shown in Figure 5.1. As shown in Figure 5.8(b), things are quite different along the leading-edge. The wider separation of trends lines when approaching the tab cutout regions indicate $\Delta\bar{P}$ is highly non-uniform in these regions (i.e. cutout areas near leading-edge). The pressures along the leading-edge near the tab cutouts are 5% to 53% higher than pressures at W_O behind the leading-edge, with the leading-edge region near the shingle center having pressures that are 2% to 36% higher (Figure 5.8(c)). For the purpose of comparing to Figure 5.4, the mean differential pressure predictions shown in Figure 5.8(a) and Figure 5.8(b) can be converted into localized predictions for the uplift pressure coefficient, $\Delta\bar{C}_p$. Figure 5.9(a) and Figure 5.9(b) show $\Delta\bar{C}_p$ at $W_O = 11.5\ mm$ behind the leading-edge and at the leading-edge, respectively, vs. the measured average leading-edge uplift displacement.

These results are fully consistent with the predicted full-field pressure distributions (Figure 5.7), where the uplift pressures on the top and bottom surfaces are

shown to increase along the leading-edge, especially near the shingle cutout regions. Figure 5.10 shows graphically the predicted flow and pressure fields in the tab cutout area that provide insight as to why the tab cutout regions undergo higher uplift displacements. Figure 5.10(a) shows the predicted streamlines overlayed with the spatially varying velocity magnitude in the tab cutout region and Figure 5.10(b) depicts the predicted flow streamlines overlayed by the local pressure field. Air in the high-pressure region below the shingle flows at high velocity through the tab cutout to reach the upper surface due to the pressure differential. As flow accelerates when passing through the tab cutout region, it exits onto the top surface to form local vortices, locally reducing pressure on the top surface. The resulting pressure and flow interactions reduce the size of the local separation bubble, focusing elevated differential pressures in this region and, as a consequence, forming local high differential pressure areas that increase uplift in this region.

In addition to the tab cutout region discussion, the general trends shown in Figure 5.8(a) and Figure 5.8(b), with a peak in $\Delta\bar{P}$ versus uplift displacement when the uplift is approximately 11.2 mm at a distance W_o behind the leading edge, require elaboration. As evident when comparing Figure 5.1 and Figure 5.2, an increase in shingle uplift results in growth of the leading-edge separation bubble on the top surface of the shingle. When shingle uplift reaches 11.2 mm, the leading-edge separation bubble extends beyond the shingle and attaches to the surface beyond the back of the shingle. Further evidence of the change in separation bubble size is shown in Figure 5.11, where flow streamlines for an inlet velocity of 67.1 m/s are obtained along the line shown in Figure 5.11(a) that extends from the leading-edge to the back of the shingle. The streamlines at $t = 3000\ s$ and

$8400\ s$ are shown in Figure 5.11(b) and Figure 5.11(c), respectively, with expansion of the recirculatory leading-edge separation bubble clearly visible as uplift increases. The top surface pressure distributions for both times are shown in Figure 5.10(d), which indicates a reduction of nearly 50% in local peak pressure on the top surface that occurs when the uplift exceeds a critical value.

Since the surface shear stress is minimized in the low-velocity separation bubble region, the shear stress distributions shown in Figure 5.7(c) can be used to indirectly visualize the evolution of the upper surface separation bubble size that occurs with increasing shingle uplift. With time as uplift increase, the reattachment point moves downstream, with nearly complete flow separation for $t = 8400\ s$. Inspection of the upper surface pressure field predictions in Figure 5.7(a) for $t = 1500\ s$ shows a heightened pressure peak at the cutout near the leading-edge, immediately followed by an abrupt decrease in the uplifting pressure when moving downstream into the contained separation bubble where the magnitude of pressure is reduced, a process that is consistent with results at later times shown in Figure 5.7. It should be noted that, though results are shown for a specific line along the shingle, similar reductions in uplift pressure occur across the entire shingle span when uplift increases beyond a critical value.

Characteristics of the leading-edge separation bubble play a vital role in the top surface pressure distribution. Though separation bubbles are generally classified as either *short* or *long*, what is most important is their effect on the pressure distribution (Häggmark 2000). Compared to inviscid flow, a *short* separation bubble shows a slight reduction in peak pressure at the leading-edge (Torenbeek 1982, Agrico de Paula 2016). Once a short separation bubble is formed behind the leading edge, a small pressure

plateau region is formed that is quickly followed by a sharp decrease in uplifting pressure before returning to a pressure distribution that is like that of inviscid flow. Once a *short* separation bubble dissipates, a *long* separation bubble is formed that further decreases the peak pressure while stretching the pressure plateau over a greater distance to eventually match the distribution observed in inviscid flow (Agrico de Paula 2016). For an uplifted shingle, the *short* dissipation bubble expands until it detaches from the shingle to form a *long* bubble that reattaches well downstream of the shingle (i.e. on the roof surface).

5.6 TEMPORAL VARIATIONS IN SHINGLE UPLIFT AND RELEVANT WIND GUST FREQUENCY

Since shingle deformation measurements were acquired at 1 Hz throughout this experiment, high frequency shingle oscillations are not measured. However, it is possible using previous data to provide estimates for the range of hurricane velocity wind gust frequencies that have the potential to affect pressure variations on shingles. As noted by Cochran (Cochran 1995), for flat asphalt shingles subjected to 10 m/s winds, the authors showed experimentally that wind gust frequency, f_g, is directly correlated with oscillations in measured uplift pressure when the $f_g^{low\ speed} \leq 12\ Hz$. These observations can be used with either the Keulegan-Carpenter number, K_c, (Keulegan 1958) or the Strouhal number, St, to estimate the relevant gust frequency for hurricane velocity winds. Since $K_c = V\ f_g^{-1} L^{-1}$, where V is the flow velocity and L is a characteristic length, and the general character of the flow fields is quite similar for both low speed and hurricane speed winds, similitude is assumed to estimate the relevant gust frequency at higher wind speed. Assuming L is related to the leading-edge vertical distance, for flat asphalt

shingles with a frontal height on the order of 3 mm, $K_c = 278$ and an estimated relevant gust frequency for 67.1 m/s winds of $f_g^{hurricane\ velocity} \leq 75\ Hz$. Thus, increasing the wind speed to hurricane velocity results in a factor of six increase in the maximum frequency of the pressure variations that can affect shingle uplift. Finally, since the step Reynold's number for flat shingles subjected to hurricane velocity winds is $Re_h = 12{,}885$ (see Chapter 5.3), the large value is indicative of low viscous forces so that a high value of K_c is indicative of fluid damping of shingle motions due to turbulent phenomena (i.e., the vortex shedding occurring as flow passes over the uplifted leading edge) as the dominant physical process in the observed shingle response, with the predicted vortex-driven damping being consistent with visual observations by the investigators of minimal shingle oscillations throughout the two hours of hurricane force winds.

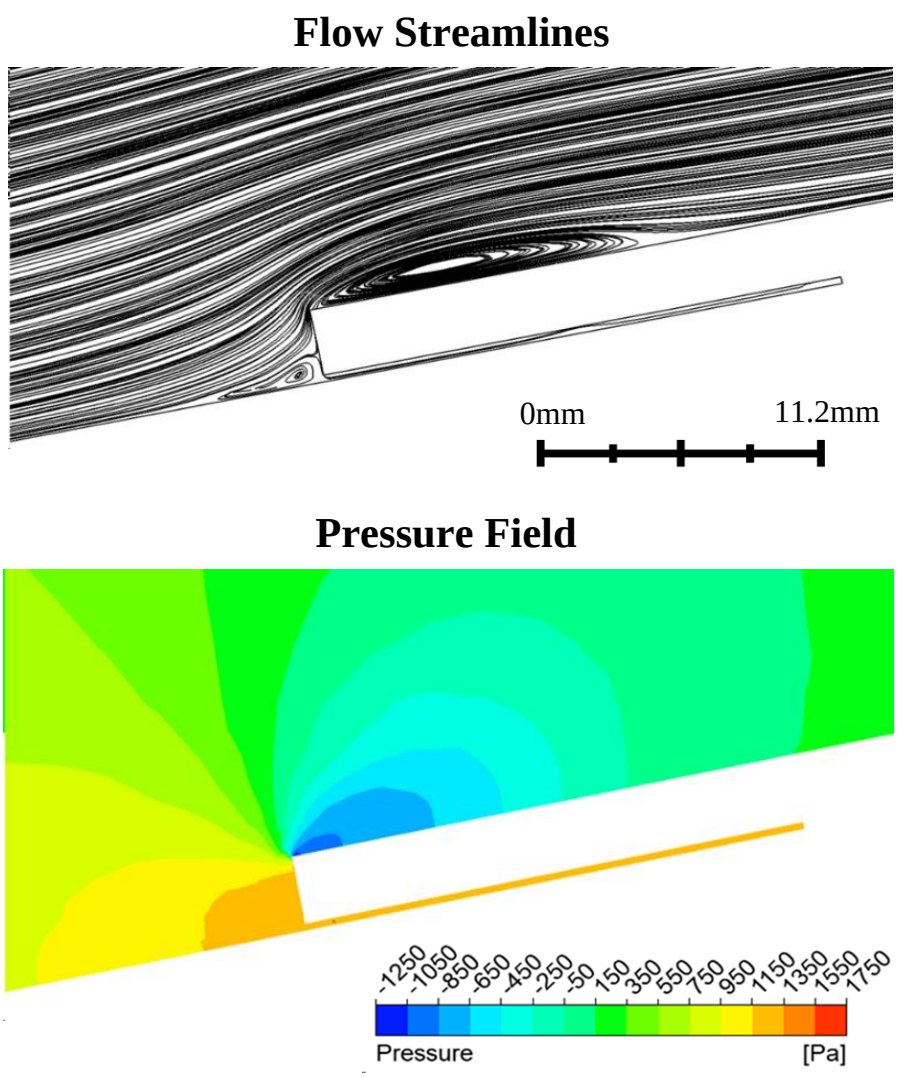

Figure 5.1 Flat shingle air flow streamlines and pressure field in z-x plane along specimen centerline ($y = 0$) at time $t = 0\ s$ for an inlet velocity of 67 m/s.

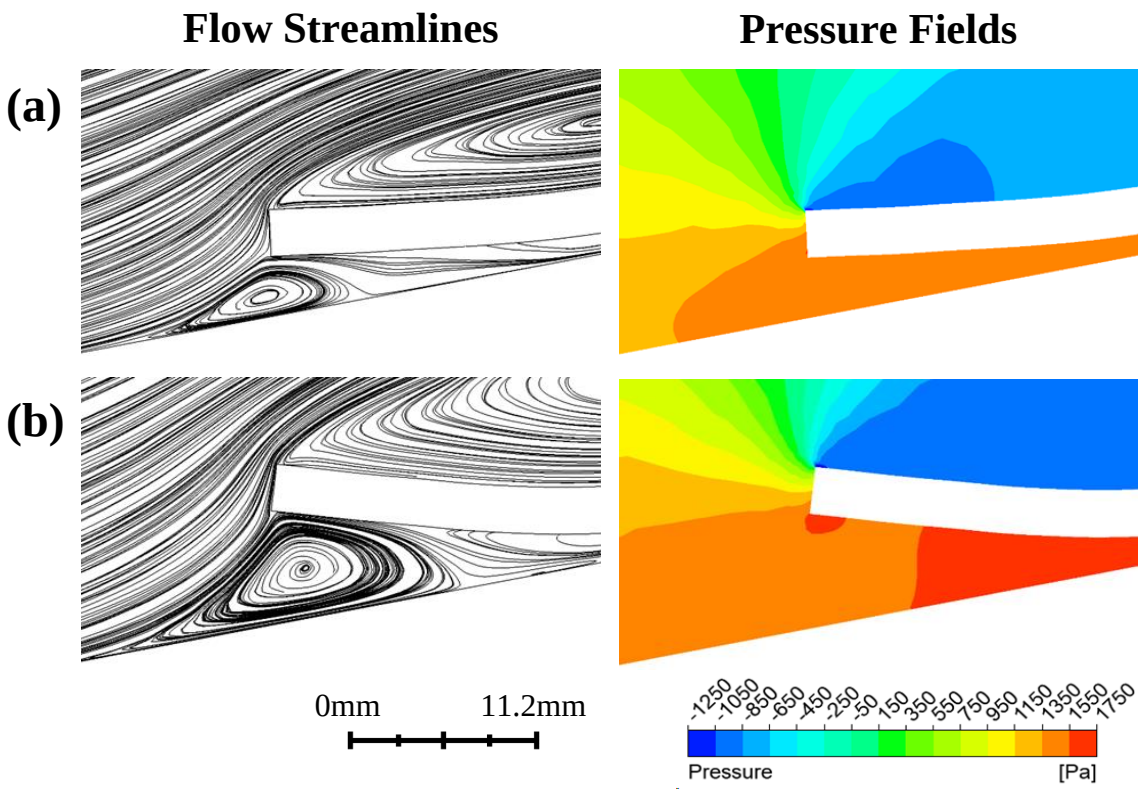

Figure 5.2 Predicted flow streamlines and and pressure distributions in z-x plane at $y = 0$ across uplifted shingle at times (a) $t = 1500\ s$ and (b) $t = 3000\ s$.

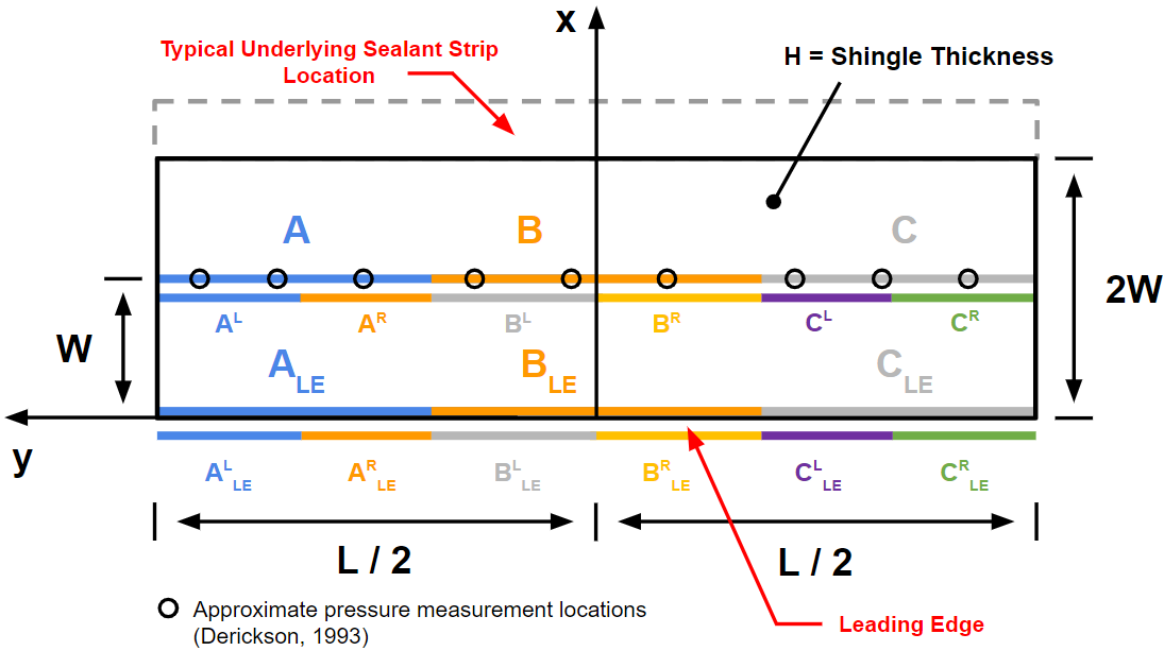

Figure 5.3 Geometry of leading-edge area for one shingle tab, with height $2W$, length L and thickness H. For Derickson's brass shingle: $W_D = 16\ mm$, $L_D = 295\ mm$ and thickness, $H_D = 2.3\ mm$. For the Owen's Corning asphalt shingle: $W_O = 11.5\ mm$, $L_O = 298.5\ mm$ and thickness, $H_O = 2.8\ mm$. Locations of pressure measurements in previous studies are also shown as circle indicating the positions of all nine pressure tabs on top and bottom of brass shingle.

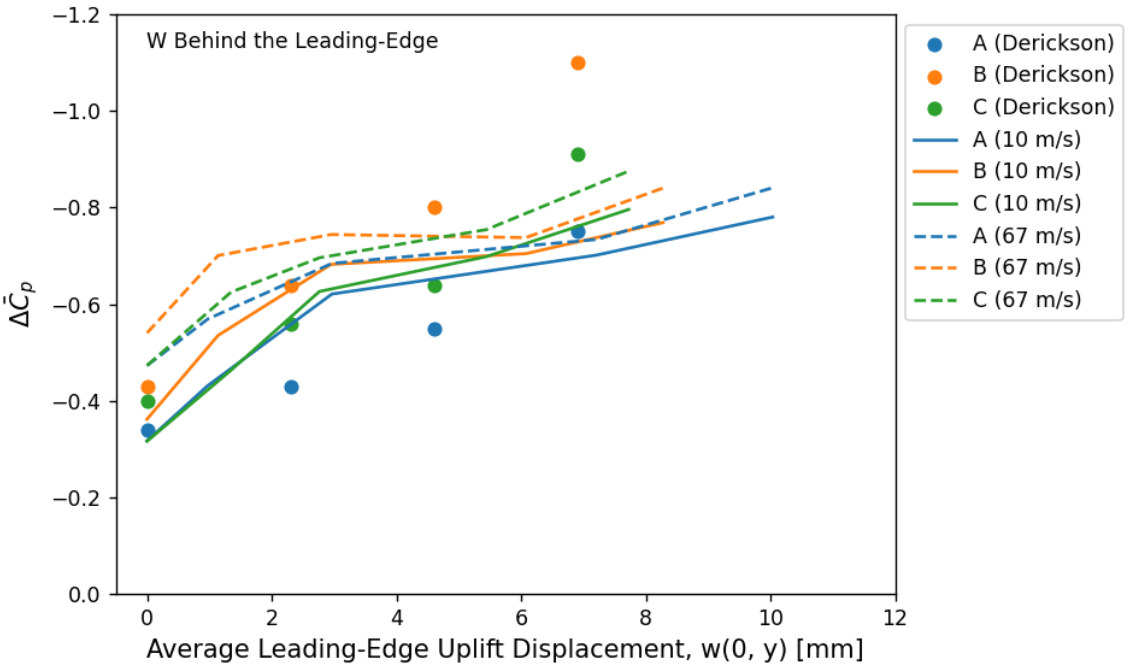

Figure 5.4 Comparison of simulation and experimental average differential pressure coefficients at the middle of the leading-edge area ($W_D = 16\ mm$ and $W_O = 11.5\ mm$ behind the leading edge) for wind speed = 10 m/s and average differential pressure.

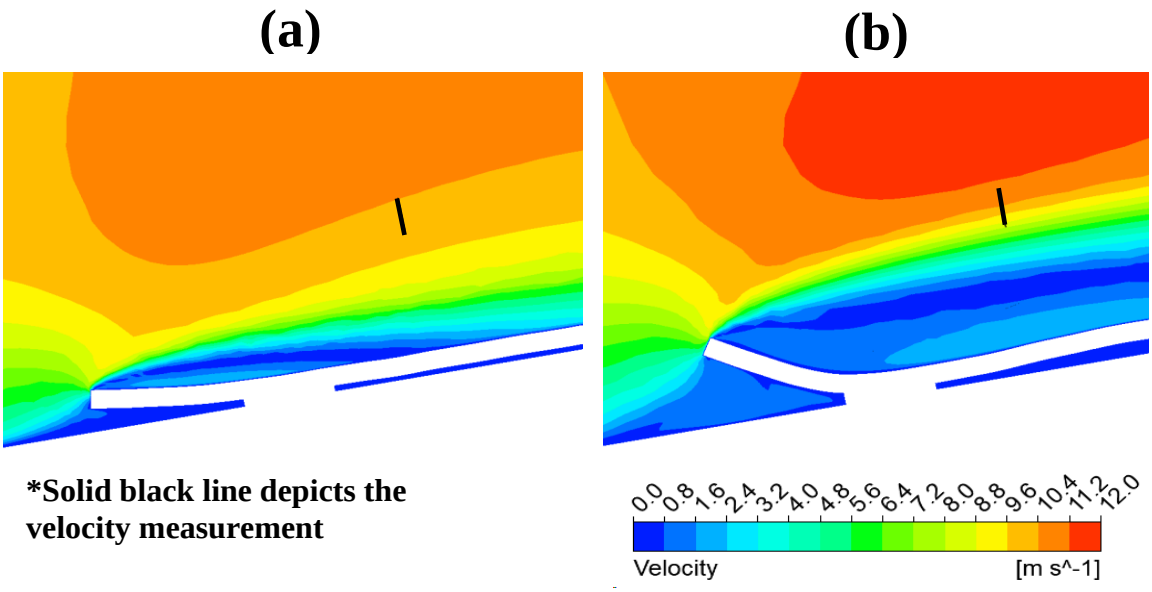

Figure 5.5 Velocity measurement location for (a) $t = 1500\ s$ and (b) $6600\ s$; using an inlet velocity of 10 m/s.

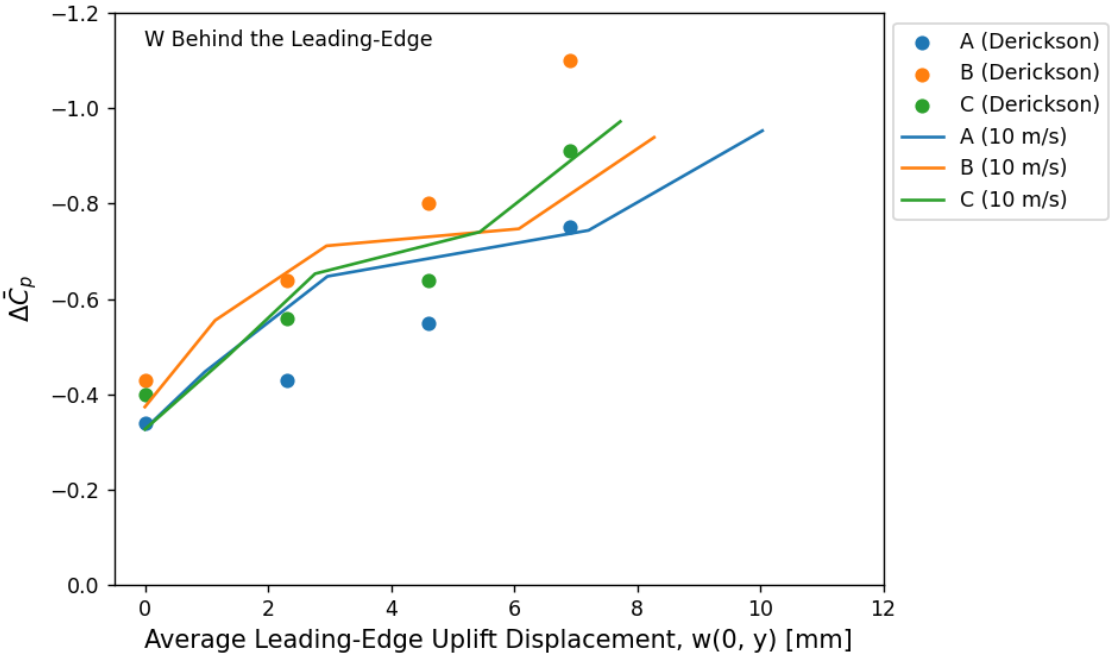

Figure 5.6 Comparison of simulation and experimental average differential pressure coefficients at the middle of the leading-edge area (wind speed = 10 m/s) with a lowered velocity measurement position. Brass shingle thickness used by Derickson, $H_D = 2.3\ mm$. Three-tab Owens-Corning asphalt shingle thickness in simulations, $H_O = 2.8\ mm$.

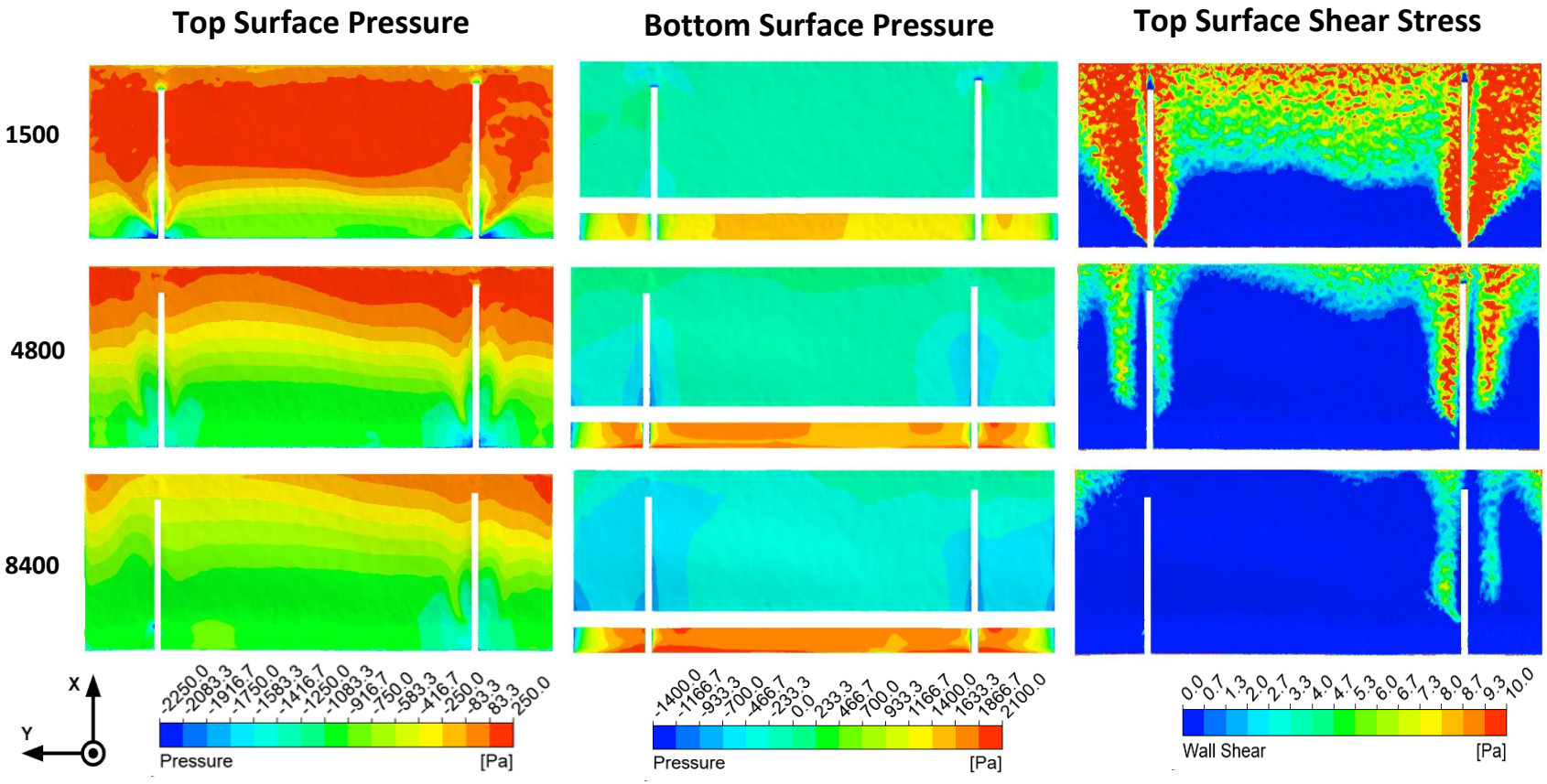

Figure 5.7 Shingle top surface pressure field, bottom surface pressure field and top surface shear stress field, τ_{xy}, for $t = 1500\ s$, $t = 4800\ s$ and $t = 8400\ s$ for a wind speed of 67.1 m/s.

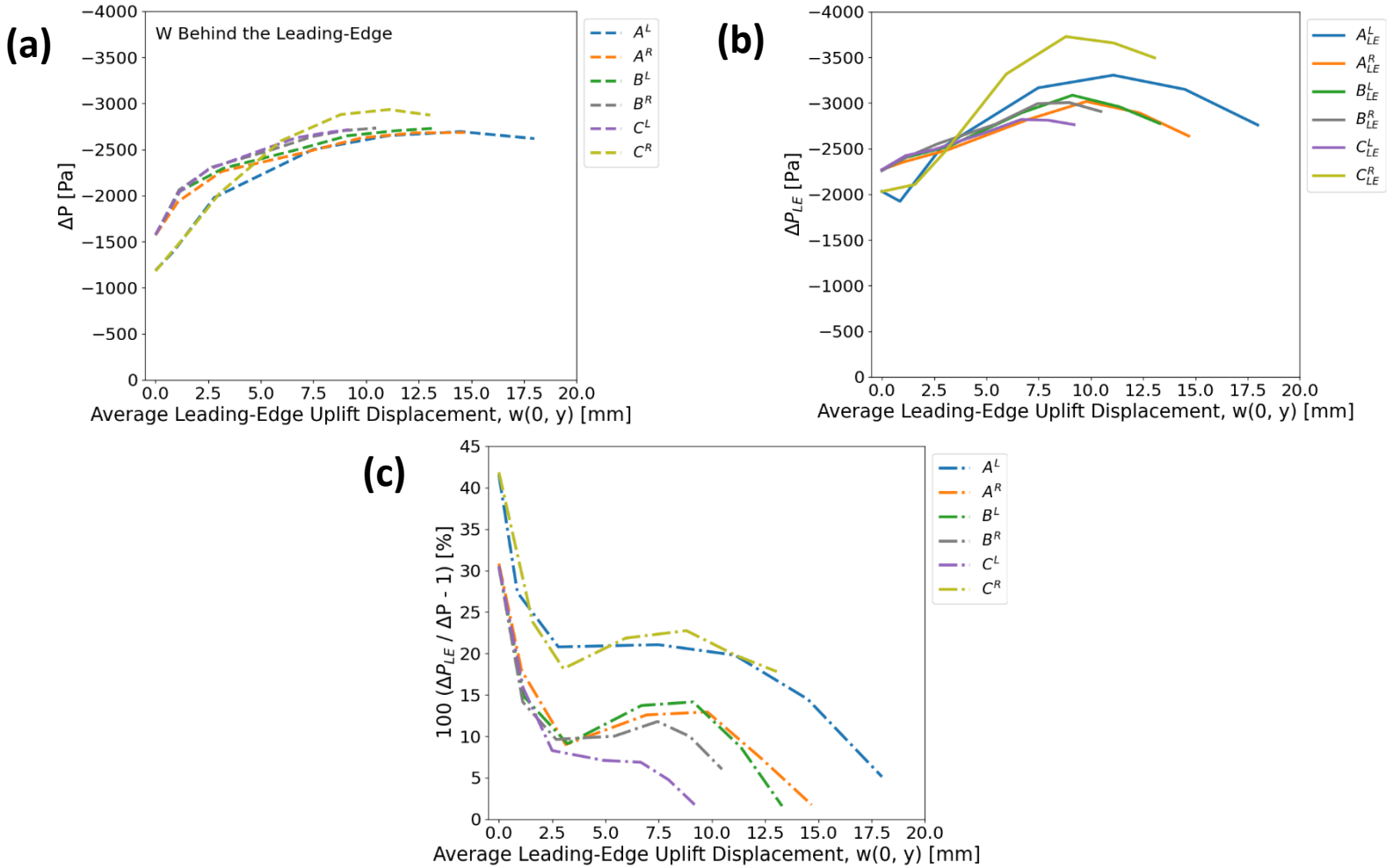

Figure 5.8 Predicted mean differential pressure versus average leading edge uplift displacement for a wind speed of 67.1 m/s (a) $\Delta\bar{P}$ at $W_O = 11.5\ mm$ behind the leading-edge area, (b) $\Delta\bar{P}_{LE}$ at the leading-edge and (c) percent difference between values of $\Delta\bar{P}_{LE}$ and $\Delta\bar{P}$.

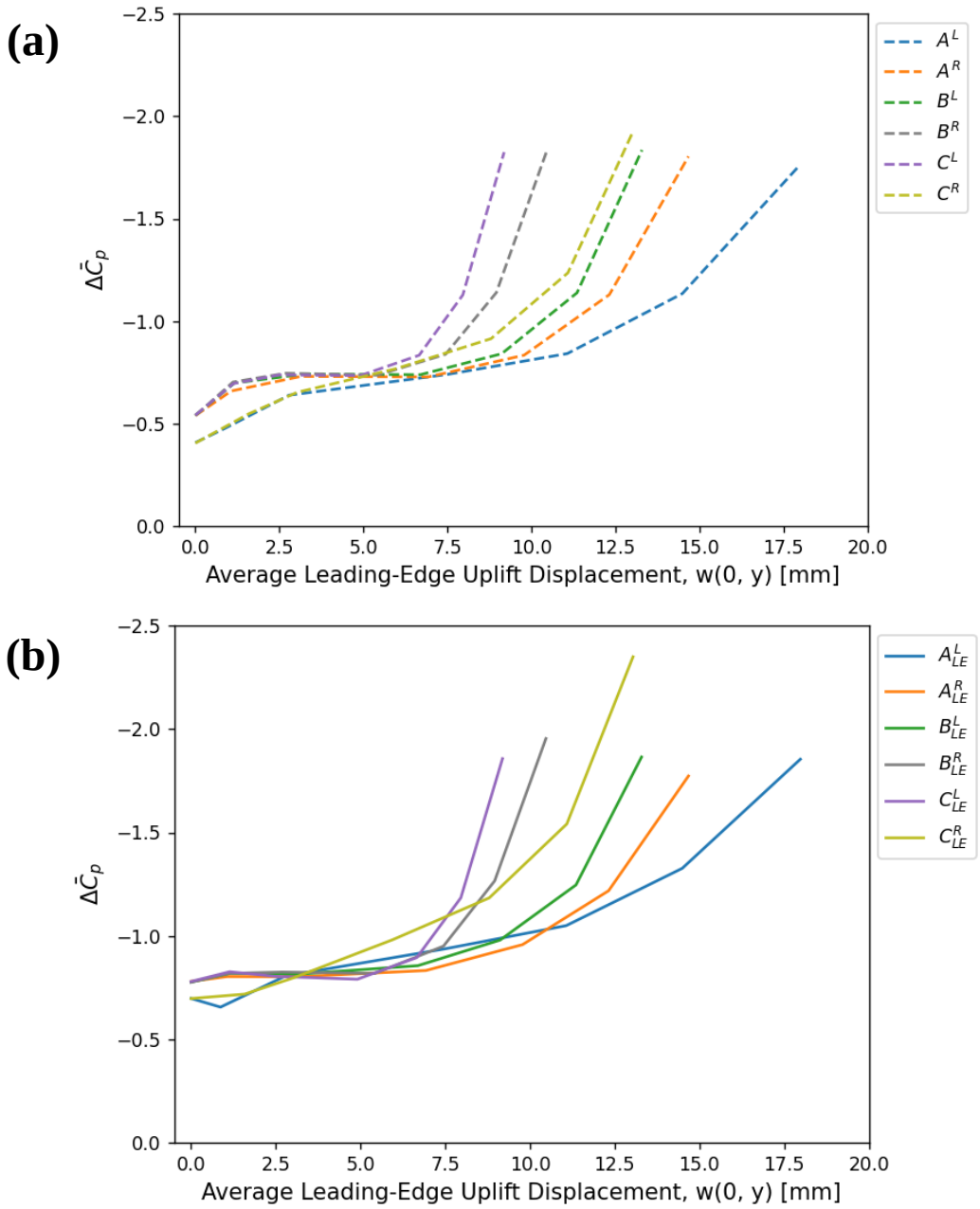

Figure 5.9 The average mean uplift coefficient, $\Delta\bar{C}_p$, at (a) $W_O = 11.5\,mm$ behind the leading-edge area and (b) the leading-edge for a wind speed of 67.1 m/s.

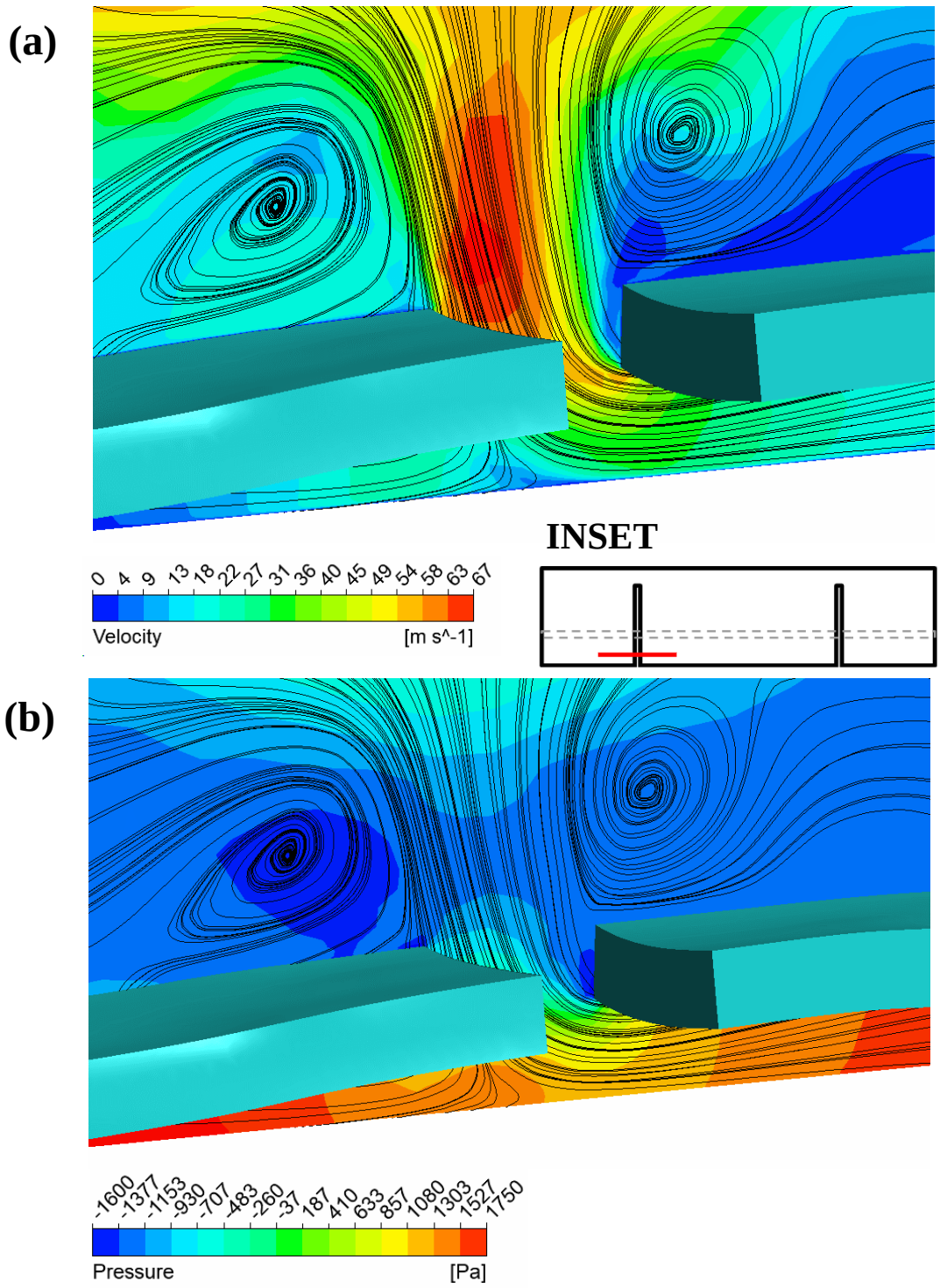

Figure 5.10 (a) Predicted flow streamlines superimposed onto a velocity magnitude distribution in z-y plane, (b) predicted flow streamlines superimposed onto a pressure distribution in z-y plane, INSET: Approximate location on the shingle for the data shown; for $t = 4800s$ and wind speed = 67.1 m/s

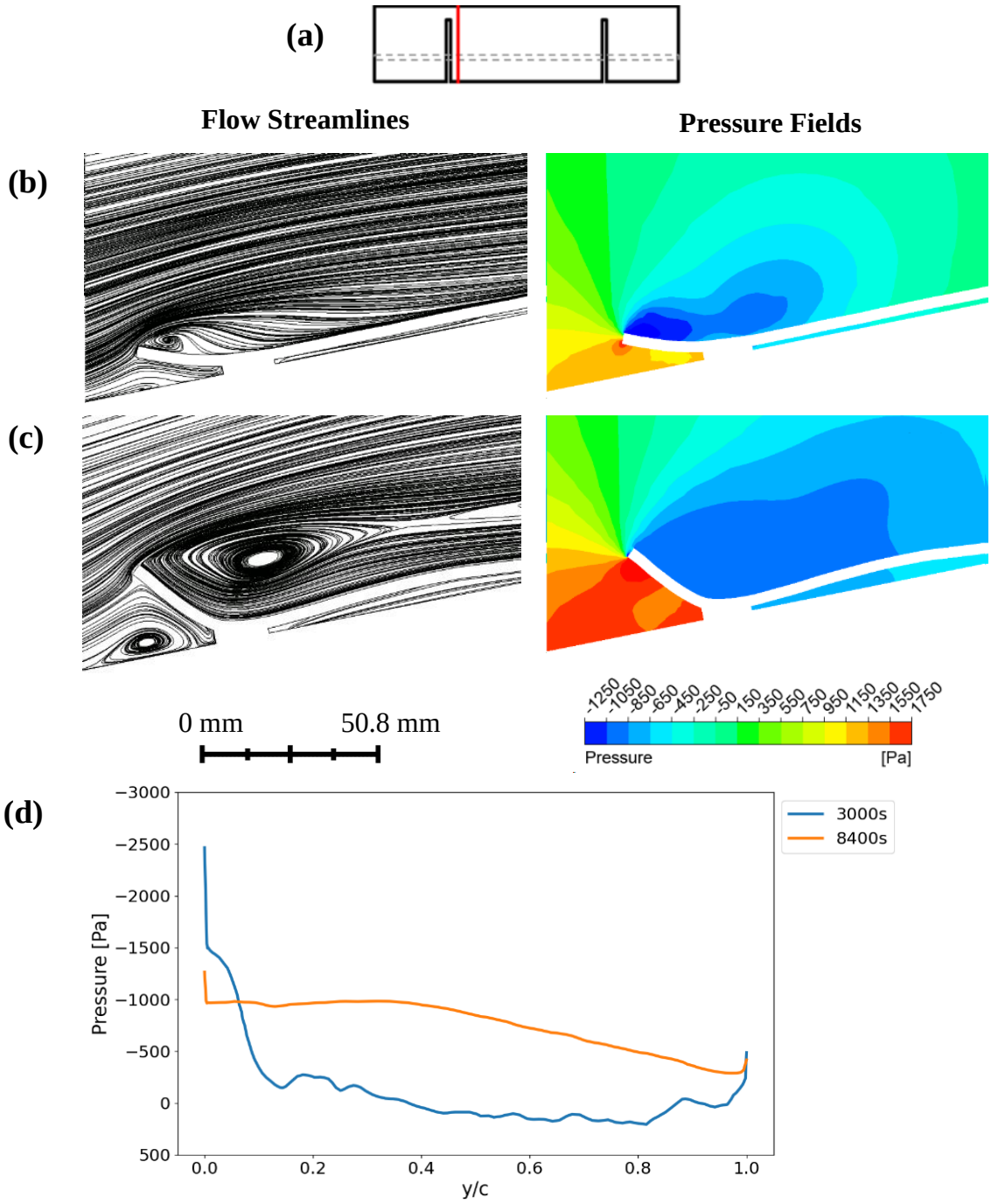

Figure 5.11 For a wind speed of 67.1 m/s, (a) line near left cutout where data is shown, predicted flow streamlines and pressure distributions in the z-x plane at (b) $t = 3000\ s$ and (c) 8400 s and (d) pressure on top surface along the line in (a)

CHAPTER 6

APPLICATION IMPLICATIONS

As noted in the introduction, modern asphalt shingles are the evolutionary form of the original individual shingle concept. Based on findings in this study, higher uplift displacements along the leading-edge and in the tab cutout regions result in higher uplift pressures in these regions. Since the authors' personal laboratory and field observations have shown that shingle uplift and separation oftentimes will initiate in the tab cutout region, one modification to the current 3-tab shingle geometry could be to consider longer, un-tabbed shingles that reduce the number of separation-prone areas. Another option would be to include sealant strips along all edges of a shingle (including the tab cutouts), providing increased resistance to uplift pressures.

Secondly, leading-edge uplift of a shingle is directly responsible for increases in uplift pressure. Thus, a second pair of modifications would focus on reducing uplift of the leading-edge portion of the shingle. Options could include (a) moving the sealant position forward, closer to the leading-edge, which not only reduces the pre-sealant area but also "stiffens" this area by reducing the unrestrained leading-edge area (Croom et al. 1 2015, Croom et al. 2 2015), (b) addition of another sealant layer behind the newly shifted layer (Croom et al. 2020, Rajan et al. 2022) and/or (c) increasing the stiffness of the shingle structure, potentially through material or thickness changes.

Thirdly, detailed results obtained in this study required measuring the full-field deformed shape of the shingle during hurricane velocity winds. The technology to obtain such measurements, StereoDIC (Sutton et al. 2009), was not available to previous researchers, but now has been used effectively for shingle systems (Ghorbani et al. 2015, Rajan et al. 2022) and is readily available today from several commercial sources (e.g. www.correlatedsolutions.com), providing unprecedented capability to visualize the deformations in both field and laboratory environments, and determine the true response of any type of shingle system. Thus, it is suggested that stereovision with StereoDIC software technology be incorporated in future research studies seeking additional understanding of the response of shingled structures and eventually into standards as an accepted measurement method.

Fourthly, the integration of StereoDIC measurements with fluid-structure computational models has important advantages. Full-field measurements of a wind-loaded, shingle system at any time can be used in computational fluid models without requiring knowledge of the continuum behavior for the complex, time-dependent, composite. This greatly simplifies each "fluid-structure" analysis since time-dependency and convergence issues are minimized by converting a time-dependent, fluid-structure interaction analysis into a discrete number of rigid structure analyses within a flow environment. In addition, direct measurement of full-field shingle response removes concerns about the ability to accurately predict the material behavior via a continuum or micro-mechanical constitutive model within the computational framework for the

shingle.[10] Also, investigators can use the direct measurements to modify the shingle system (e.g. material, sealant, geometry) and rapidly and accurately quantify full-field shingle response in laboratory-scale, high wind loading conditions to assess the overall performance of the modified shingle structure.

[10] As an example of the issues faced in developing such a model, the bending response of an asphalt shingle is directionally dependent due to the interaction of the surface granules when the shingle deforms upwards.

CHAPTER 7

FUTURE TECHNICAL DIRECTIONS

Simulations in this work are focused on prediction of the full-field pressure distribution for the as-measured shingle shapes, providing a framework for developing a complete shingle simulation platform that incorporates independent experimental measurements for validation. The flow chart shown in Figure 7.1 provides an overview of the technical areas and their interrelationships envisioned to develop a comprehensive, validated simulation platform for development and rapid assessment of modifications in future shingle-sealant roofing systems.

Initially a sealant material is selected, leading to a series of baseline experiments to obtain (a) sealant traction separation laws $(\boldsymbol{t}, \delta)$ as a function of the bonding temperature, T, pressure, p, and time, t, and (b) mechanical properties of the shingle. These properties are then incorporated in a modified shingled roof model. The modified shingled roof structure is incorporated in a fluid-structure simulation model that is visually like the one shown previously, but with the added capability to simulate time-dependent deformations of both the shingle and sealant during wind loading. For sealant layers that remain bonded throughout the simulation, conditions in the sealant can be compared to independent experimental traction-separation measurements for the same

(T, p, t) process conditions to confirm that model predictions are consistent with experimental observations.

When this is confirmed, a series of additional simulations are then performed with different traction-separation laws to predict the range of (T, p, t) process conditions that result in adequate bonding during wind loading. For sealant layers that are predicted to separate and fail during wind loading, a select number of additional full-scale wind experiments on shingled roof systems with sealant layers that are processed with the same (T, p, t) conditions are performed to confirm model predictions are consistent with experimental observations and to provide guidance as to the range of (T, p, t) process conditions that will result in adequate bonding during wind loading.

Once the simulation platform has been validated, the effect of a broad range of material and structural changes can be determined efficiently and those combinations that provide the highest level of performance can be identified and confirmed through a reduced number of full-scale wind experiments.

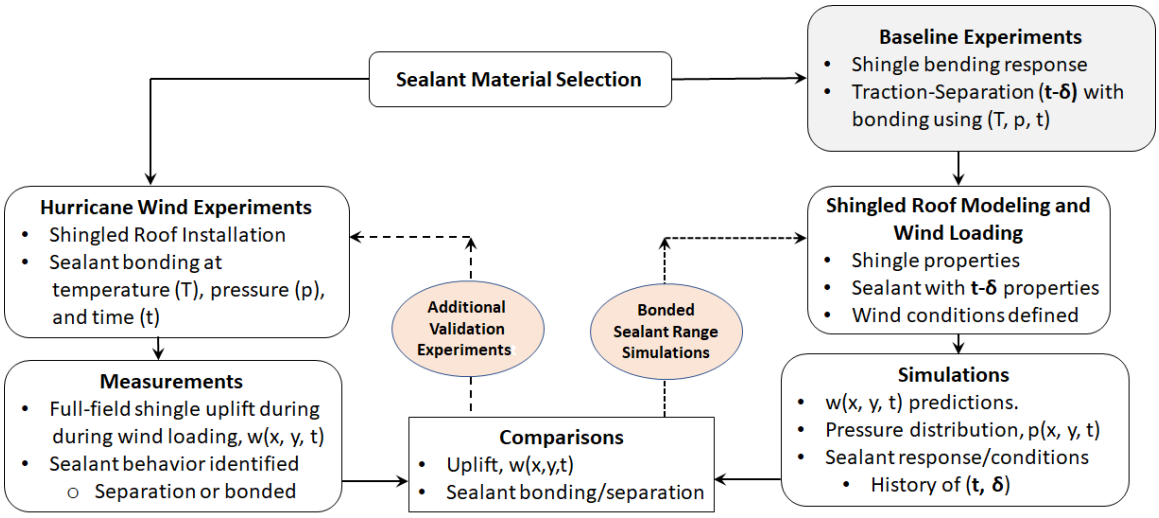

Figure 7.1 Flow chart overview of the technical areas and their interrelationships envisioned to develop a comprehensive, validated simulation platform for development and rapid assessment of modifications in future shingle-sealant roofing systems.

CHAPTER 8

CONCLUSIONS

A novel hybrid experimental-computational fluid-structure interaction methodology is developed and used successfully to determine the flow fields and resulting full field pressure distributions on three-tab asphalt roofing shingles subjected to hurricane winds. Using stereovision and StereoDIC software, the full-field deformed shapes of a three-tab asphalt shingle subjected to hurricane velocity wind loading are measured at 1 Hz for over two hours. Converting the measured three-dimensional full-field positions of all points on the shingle at multiple times during wind loading into a format compatible with the Fluent CFD platform, detailed simulations of fluid flow across the as-measured deformed shingles were completed.

For low-speed winds and small uplift, results from these studies indicate that CFD predictions of uplifting pressures are in reasonable agreement with prior experimental data. Extending the predictions to hurricane velocity winds, simulations indicate the largest pressures and shingle uplifts occur in the region upstream of the bonded sealant layer. Simulations clearly show both the temporal and spatial evolution of both front surface and leading-edge separation bubbles that are the primary physical processes

controlling the uplifting pressure fields, with the measured three-dimensional asphalt shingle shapes introducing complex flow conditions and non-linearities in the leading-edge and tab cutout regions. For short distances behind the leading edge, simulations show essentially span-wise uniformity in the instantaneous pressure fields for all shingle shapes. Along the leading-edge of the shingle, simulations show the highest differential pressures ($\Delta P_{max} = 3.7\ kPa$) and largest uplifts ($w_{max} = 18.2\ mm$) occur at the tab cutouts. The simulations also show that the maximum pressure occurs for a slightly smaller uplift of 11.2 mm, with additional uplift corresponding to lower pressures as changes in separation bubble geometry occur.

REFERENCES

Abraham H (1918) Asphalts and Allied Substances: Their Occurrence, Modes of Production, Uses in the Arts and Methods of Testing, D. Van Nostrand Company, New York, NY.

Agrico de Paula A (2016) The Airfoil Thickness Effects on Wavy Leading-edge Phenomena at Low Reynolds Number Regime, University of São Paulo, São Paulo, Brazil.

ANSYS Fluent Tutorial Guide (2017). ANSYS, Inc., Canonsburg, PA.

ANSYS Fluent Theory Guide (2017). ANSYS, Inc., Canonsburg, PA.

ARMA (2014) Residential Asphalt Roofing Manual: Design and Application Methods, Asphalt Roofing Manufacturers Association, Washington, D.C.

ASTM D7158 (2015, 2016) Standard Test Method for Wind Resistance of Asphalt Shingles (Uplift Force/Uplift Resistance Method), ASTM International, West Conshohocken, PA.

Cash CG (1995). Asphalt Roofing Shingles, 11th Conference on Roofing Technology, Gaithersburg, MD.

Cermak, JE, 1981. Wind Tunnel Design for Physical Modeling of Atmospheric Boundary Layer, ASCE J. Engineering Mechanics, 107 (3) 523-642.

Cermak JE, Peterka JA and Hosoya A (1983) Wind Tunnel Study of Wind Pressures on Roofing Shingles. Colorado State University Report CER83-84JAP-JEC-AH21 for Owens-Corning Fiberglass Corporation.

Cermak JE, Peterka JA, Cochran LS, Derickson RG (1991) Mean and Gust Wind Speeds on Roofs of Low Rise Buildings, ARMA Report, CSU 2-9 8350.

Cermak JE, Peterka JA, Derickson RG and Cochran LS (1991) Prediction of Wind-Induced Uplift of Asphalt Roofing Shingles on Low-Rise Buildings, ARMA Year 1 Report, CER91-92JEC-JAP-RDG-LSC-5 CSU 2-9 8350 1-130.

Chen P-W, Bai C-J, Wang W-FC (2016) Experimental and Numerical Studies of Low Aspect Ratio Wing at Critical Reynolds Number, European Journal of Mechanics B/Fluids, vol. 59, 161-168.

Cochran LS, Peterka JA and Cermak JE (1995) Wind Tunnel Study of Shingles on a Roof, ARMA Final Report CER94-95LSC-JAP-JEC2 CSU 2-9-8350 1-91.

VIC-3D Version 9, Correlated Solutions Incorporated, 121 Dutchman Blvd, Columbia, SC 29063; www.correlatedsolutions.com/vic-3D/ .

Croom BP, Sutton MA, Zhao X, Matta F, Ghorbani R, Aleshin A (2015) Modeling of Asphalt Roof Shingle-sealant Structures for Prediction of Local Delamination Under High Wind Loads, Engineering Structures, vol. 96 100-110 (2017).

Croom BP, Sutton MA, Zhao X, Matta F, Ghorbani R, Aleshin A (2015) Corrigendum to Modeling of Asphalt Roof Shingle-sealant Structures for Prediction of Local Delamination Under High Wind Loads, Engineering Structures, vol. 122 350-354.

Croom BP, Rajan S, Matta F, Aleshin A, Myers T, Sutton MA (2020) Modeling of Asphalt Roof Shingle Structures with Dual Sealant Strips; Optimization for Improved Delamination Resistance Under High Wind Loads, Journal of Building Engineering, vol. 30 101266.

Derickson RG, Peterka JA, Cermak JE, Cochran LS (1993) ARMA Year 2 Report: Wind-Tunnel Study of Shingles on a Roof, CER92-93RDG-JAP-LSC6; CSU 2-9 8350 1-118.

Graziani A, Kerhervé F, Martinuzzi, RJ, and Keirsbulck, L (2018) Dynamics of the Recirculating Areas of a Forward-Facing Step, Experiments in Fluids, vol. 59, no. 10, 2018.

Ghorbani R, Zhao X, Matta F, Sutton, MA, Kidane A, Liu, Z-Z, Cope A, Reinhold T (2015) Feasibility of Non-Contacting Measurement of Wind-Induced Full-Field Displacements on Asphalt Shingles. In: Jin H., Sciammarella C., Yoshida S., Lamberti L. (eds) Advancement of Optical Methods in Experimental Mechanics, Volume 3. Conference Proceedings of the Society for Experimental Mechanics Series. Springer, Cham.

Häggmark C (2000) Investigations of Disturbances Developing in a Laminar Separation Bubble Flow, Royal Institute of Technology, Stockholm, Sweden.

IBHS (2009) Hurricane Ike: Nature's Force vs. Structural Strength, Insurance Institute for Business & Home Safety, Tampa, FL.

Brown-Giammanco, TM, Giammanco IM, Pogorzelski H (2018) Hurricane Harvey Wind Damage Investigation, Insurance Institute for Business & Home Safety.

Keulegan, G. H.; Carpenter, L. H. (1958), Forces on Cylinders and Plates in an Oscillating Fluid, Journal of Research of the National Bureau of Standards, 60 (5): 423–440.

Menter FR, Lechner R, Ansys German GmbH, Matyushenko, A, NTS, St. Petersburg (2020) Best Practice: Generalized k-ω Two-Equation Turbulence Model in ANSYS CFD (GEKO), ANSYS Inc., Canonsburg, PA.

Peterka JA, and Cermak JE (1983) Wind-Tunnel Study of Wind Resistance of Roofing Shingles, Colorado State University CSU Project 2-95470 1-70.

Peterka JA, Cermak JE, Cochran LS, Cochran BC, Hosoya N, Derickson RG, Harper C, Jones J, Metz B (1997) "Wind Uplift Model for Asphalt Shingles." Journal of Architectural Engineering, vol. 3, no. 4, 147–155.

Rajan-Kattil S, Myers T, Sutton MA, Boozer, M, Kidane A, Ghorbani, R, Matta F, Full-Field Shingle Uplift Measurements Using Stereodic: Comparison Of Single And Double Sealant Three-Tab Shingle Responses When Subjected To Hurricane Velocity Winds, Journal of Wind Engineering and Industrial Aerodynamics (in press).

Sherry MJ, Jaconoa DL, Sheridan J (2009) Flow Separation Characterisation of a Forward Facing Step Immersed in a Turbulent Boundary Layer, Monash University, Victoria, Australia.

Sutton MA, Orteu JJ and Schreier HW (2009) Image Correlation for Shape, Motion and Deformation Measurements, Springer ISBN: 978-0-387-78746-6.

Torenbeek E (1982) Synthesis of Subsonic Airplane Design, Springer-Science+Business Media, B.V.

Yang ZG, Yang W, Jia Q (2010) Ground Viscous Effect on 2d Flow of Wing in Ground Proximity, Engineering Applications of Computational Fluid Mechanics, vol. 4, no. 4, 521-531.

APPENDIX A

SHAPE AND DEFORMATION MEASUREMENTS USING STEREODIC FOR FULL-SIZE THREE-TAB SHINGLES SUBJECTED TO HURRICANE VELOCITY WINDS

To obtain experimental data for CFD simulations, two rows of three-tab asphalt shingles are employed using a modified version of ASTM D7158 (2016) to activate the sealant strip. The as-manufacture shingled roof facsimile is shown in Figure A.1. In this work, the two three-tab shingle rows are overlapped for bonding, placed on a sacrificial plywood surface, moved into a large oven and heated at 70^{o} C for 16 hours to ensure full bonding of the sealant strip. The bonded shingles and plywood surface are then removed from the oven and cooled to room temperature. The bonded shingles are carefully transferred to a new 19.05mm thick plywood panel and attached using a modified version of the manufacturer's instructions. Specifically, (a) the lower row of shingles is permanently bonded to the plywood panel to focus attention on the behavior of the central tab in the 2^{nd} row of shingles and (b) the upper row of shingles is attached using screws to minimize damage associated with the attachment process.

Once the shingled roof panel is manufactured, the entire panel is bolted onto the steel test stand shown in Figure A.2(c). In this work, the upper test stand surface is tilted into the wind by 10^{o}, consistent with ASTM D3161. As noted in previous work (Rajan,

2022), the steel test stand and plywood panel are essentially rigid when subjected to wind speeds up to 87 m/s (190 mph). The maximum displacements of any point on the bolted plywood panel less than 0.100 mm at maximum speed. Thus, all measured displacements for the shingles represent to a close approximation shingle response.

To subject the shingled roof facsimile to hurricane velocity winds, the sub-sonic wind tunnel shown schematically in Figure A.2(a) is employed. To improve uniformity in the winds exiting the tunnel, within the settling chamber of the wind tunnel are three flow stabilization screens. The first screen with a rectangular grid of lines and 2.03mm x 2.03mm square gaps is shown in Figure A.2(b). Immediately after this screen is a 2nd screen with a horizontal grid of lines that has 914.4mm x 22.9mm gaps spanning the chamber. The last screen is a vertical grid of lines with 22.9mm x 914.4mm gaps that also spans the chamber. As shown in Figure A.2(c), the test stand with the shingled roof facsimile roofing panel is bolted to the reinforced concrete floor and and placed at the wind tunnel exit, a configuration that is similar the setup of Derickson et al. shown in Figure A.3.

To obtain full-field shingle deformation measurements throughout the hurricane velocity wind loading process, the stereo camera system shown at the top of Figure A.2(d) is used. The stereo system is mounted above the wind tunnel to acquire stereo images of the shingled panel without significant buffeting of the system due to the hurricane velocity winds during wind loading. In this study, all shingle measurements and thus all simulations, are for wind velocity exiting the tunnel that is perpendicular to the leading-edge of the shingle (skew angle is zero).

Following the procedure described in detail in previous studies (Rajan, 2022), stereo image pairs of the shingled roof are acquired using VIC-Snap software (www.correlatedsolutions.com) at 1 Hz while the wind speed, as measured by a pitot tube at the end of the wind tunnel, is (a) increased from 0 to 26.8 m/s and held for 600 seconds, (b) increased from 26 m/s to 40.2 m/s and held for 600 seconds and (c) increased to 67.1 m/s and held constant for the remainder of the experiment[11]. Stereo digital image correlation analysis of the high contrast shingle images[12] (see the bottom shingle in Figure A.4 to visualize contrast in the speckle image) was performed independently in this study using VIC-3D software (www.correlatedsolutions.com) with the analysis parameters shown in Table A.1. Figure A.4 shows the uplift displacement field measured after 4800 seconds of exposure to hurricane velocity winds.

Table A.1 StereoDIC analysis parameters and stereo camera specifications

Subset size	45x45 pixels
Step size	5 pixels
Subset weighting	Center-weighted Gaussian
Strain filter size	5x5 data points (area of 25x25 pixels)
Camera	5 MP CMOS Point Grey
Lens	35mm Schneider
Field of view	500 mm x 500 mm
Average speckle size	2.85 mm
Magnification	0.19 mm/pixel

[11] Previous studies have shown that wind speeds below 40.2m/s for 20 minutes did not not induce measurable shingle uplift.

[12] The typical procedure to obtain a high contrast random on a specimen surface is to lightly coat the surface with white paint and then overspray with black paint. However, recent publications (Ghorbani et al. 2015, Rajan et al. 2022) have shown that even light coats of paint stiffen the shingle so that its displacements are reduced relative to the unpainted shingle. Thus, painting is not advisable and was not used in this work or previous image correlation measurement experiments on asphalt shingles.

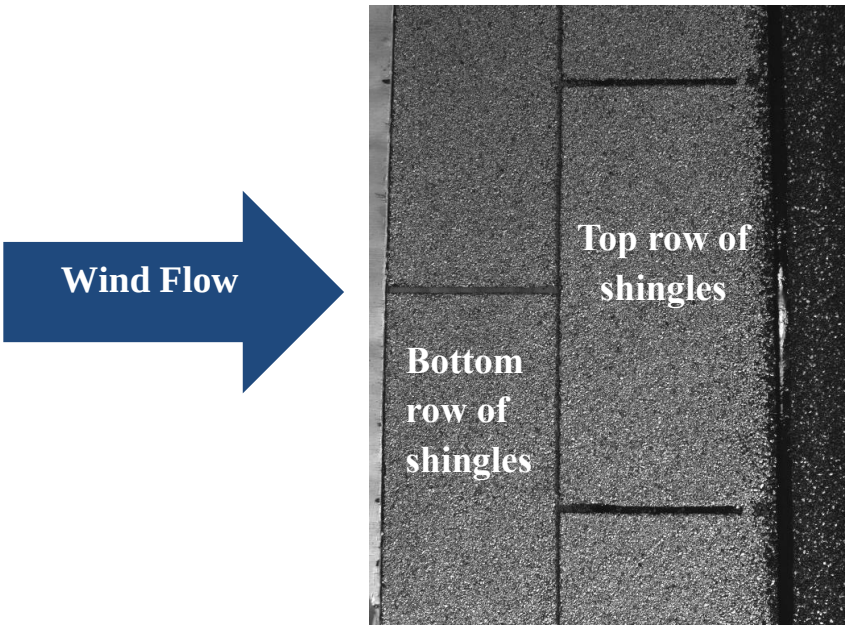

Figure A.1 Photograph of two rows of full-sized shingles attached to plywood base. Dimension for shingled plywood system is 0.60 m x 0.60 m. Bottom row of shingles are permanently bonded to plywood base, with mid-tab of top row being the focus of the studies. Details for experimental program given in previous publication (Rajan et al, 2022).

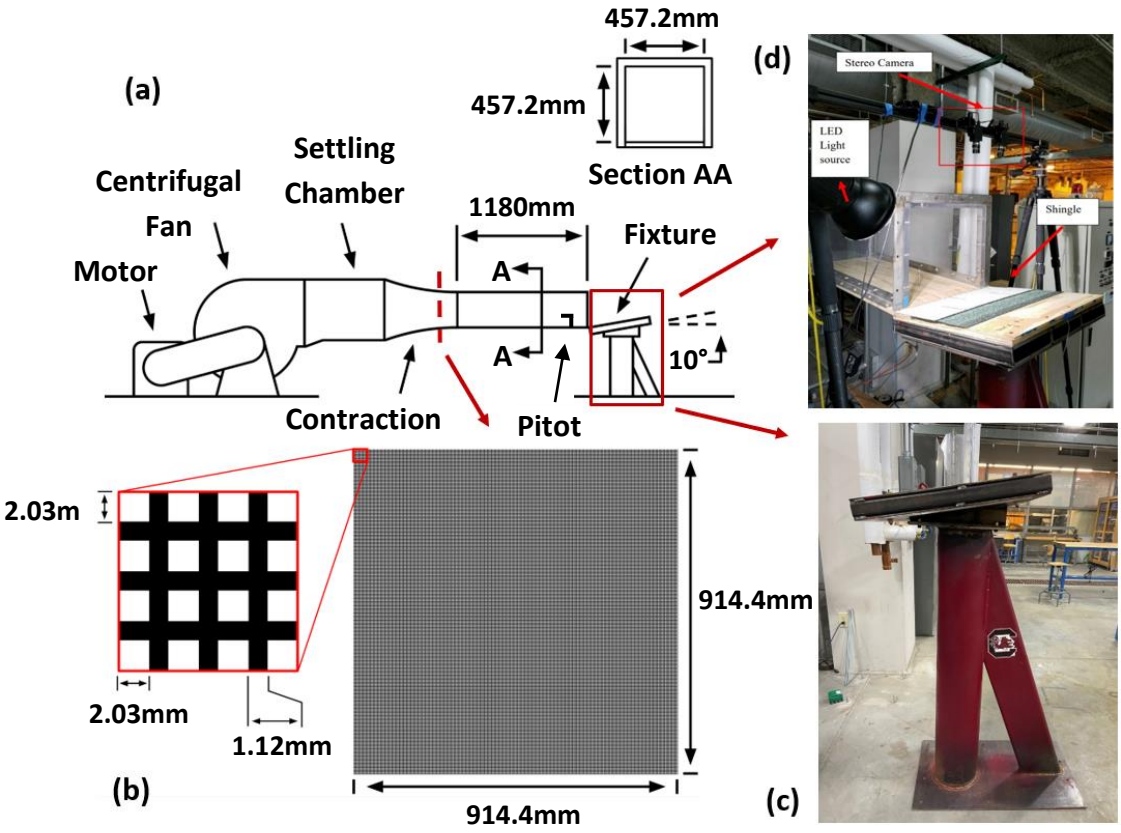

Figure A.2 Experimental setup including (a) Sub-sonic wind tunnel with converging flow section; (b) INSET BOTTOM LEFT: First screen in settling chamber to improve uniformity of flow; (c) INSET: Photo of as-manufactured, stiffened shingle test stand with 10^{o} inclined shingle mounting plate; (d) INSET TOP RIGHT: Photo of stereovision system mounted above test stand for imaging of shingles. Additional details in Rajan et al. 2020.

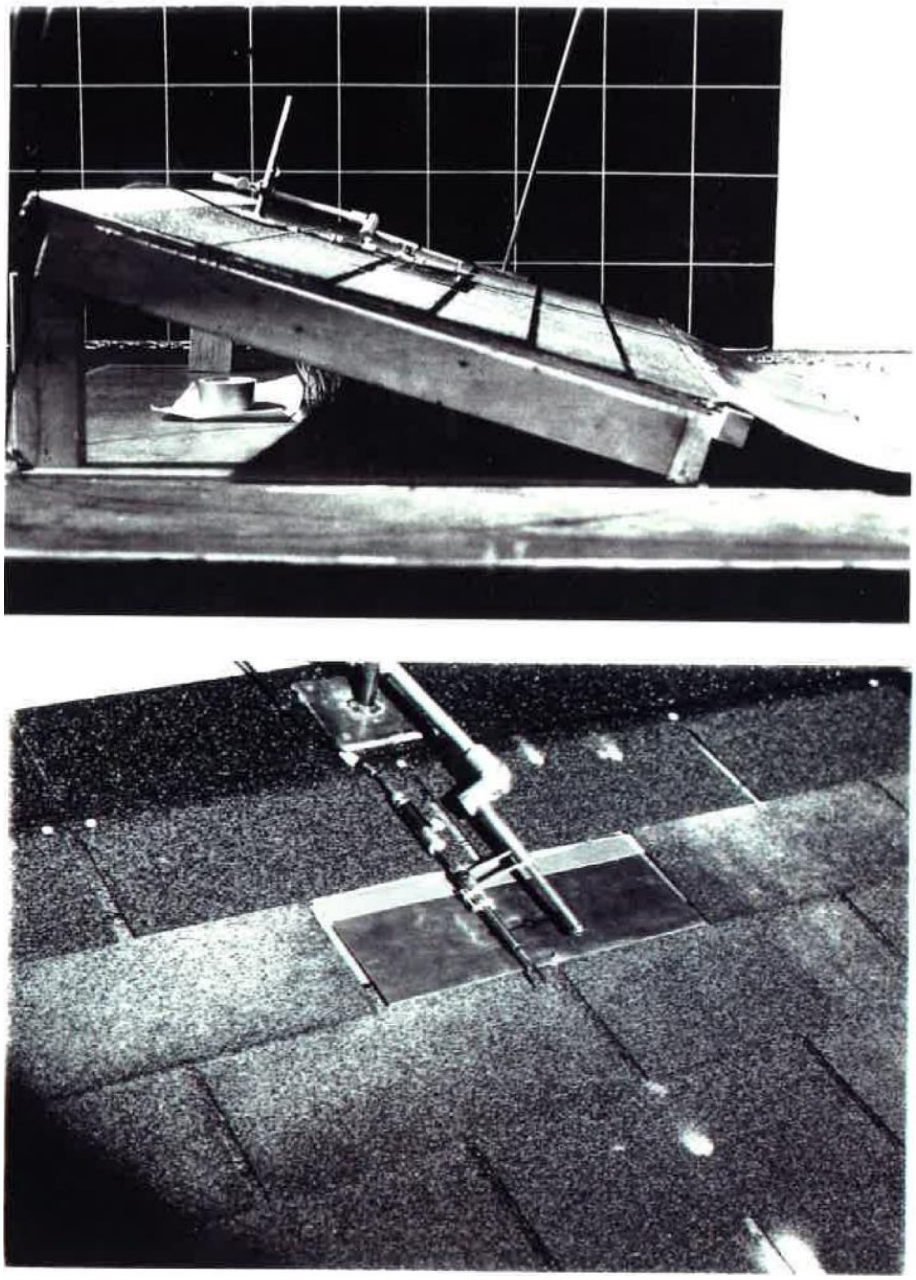

Figure A.3 Experimental setup from Derickson et al. (1993) including a floor mounted roofing structure with a brass shingle.

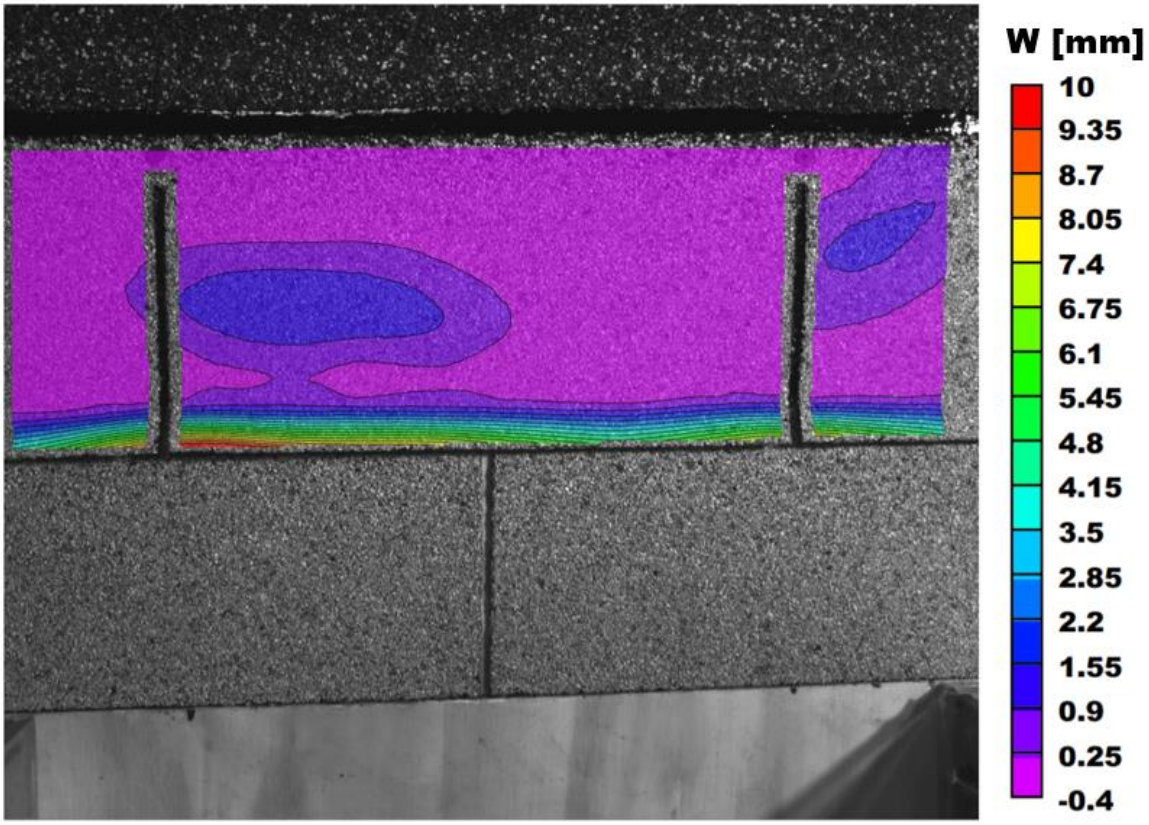

Figure A.4 Upward displacement, $w(x, y)$, at $t = 4800\ s$ experiment time (wind speed = 67.1 m/s).

APPENDIX B

COMPUTATIONAL CHARACTERIZATION OF FLOW CONDITIONS INCIDENT ON SHINGLED ROOF SPECIMEN

B.1 PREDICTED EXIT WIND VELOCITY PROFILE FOR A RANGE OF TURBULENCE INTENSITIES AND VISCOSITY RATIOS

Since the shape of the incident velocity profile for the wind tunnel studies in this work is an important aspect of fluid-shingle interaction studies, and the authors did not perform extensive velocity measurements, the authors utilized the ANSYS-Fluent simulation platform with the measured mean outlet velocity to predict the incident velocity profile. To do so, a 2D computational model of the wind tunnel was constructed to include the contracting section of the wind tunnel for a more accurate representation of flow development along the relatively short straight section. As shown in Figure B.1, the wind exits the tunnel and immediately passes over the shingle test deck before flowing into the plenum region that has a large volume which is open to outside air.

Since experimental data regarding the flow quality was not acquired, simulations were performed for various combinations of turbulent intensity, I, and turbulent viscosity ratio, $\mu t/\mu$. The combinations used in our series of simulations are shown in Table B.1. For each case, a line sample is drawn to acquire the turbulence kinetic energy and mean velocity at 95% of the length along the test section, corresponding to a location that is

just before the junction of the wind tunnel and the shingle test deck. The turbulence intensity, I, is calculated using Equation B.1 where $\overline{U}$ is the mean velocity and u' is the root-mean-square of the turbulent velocity fluctuations defined by Equation B.2 where k is the turbulence kinetic energy.

$$I = \frac{u'}{\overline{U}} \tag{B.1}$$

$$u' = \sqrt{\frac{1}{3}(u'^2_x + u'^2_y + u'^2_z)} = \sqrt{\frac{2}{3}k} \tag{B.2}$$

The turbulence intensity and velocity profiles for each case are shown in Figure B.2(a) and Figure B.2(b), respectively. Inspection of Figure B.2(a) and Figure B.2(b), where all the profiles have collapsed onto a single line, show that altering the inlet conditions for both intensity and viscosity ratio have negligible effect on the flow characteristics downstream at the tunnel exit. To confirm that I and $\mu t/\mu$ over the range investigated does not affect appreciably the predicted pressure differences along the leading-edge region of the shingle, 3D simulations for a flat shingle with wind velocity of 67.1 m/s were performed with $I = 10\%$, $\mu t/\mu = 20$ and $I = 5\%$, $\mu t/\mu = 10$. The predicted pressure differences for the leading-edge areas A^L, A^R, B^L, B^R, C^L and C^R for both cases are shown in in Figure B.3.

B.2 COMPARISON OF EXIT WIND VELOCITY PROFILE TO A FULLY DEVELOPED PROFILE

Since previous studies employed meteorological wind tunnels to obtain fully developed wind velocity profiles, the authors performed additional 2D simulations to compare the wind velocity profile for our experimental setup shown in Fig. B.2(b) to a

fully developed boundary layer profile. To achieve a fully developed flow field, the second computational domain is a fictional wind tunnel with an extended test section length, with data acquired approximately 0.6 m prior to the exit region. Figure B.4(a) and Figure B.4(b) compares the predicted fully developed and incident shingled test specimen (a) turbulence intensity profiles and (b) wind velocity profiles, respectively.

B.3 PREDICTED SHINGLE PRESSURE FOR A FULLY DEVELOPED AND PREDICTED WIND VELOCITY PROFILES

Prescribing the fully developed flow profile shown in Figure B.4(b) across the entire width of the wind tunnel shown previously and performing 3D fluid flow simulations for a 10^o inclined flat shingle structure with wind velocity of 67.1 m/s, the uplift pressure fields on the shingle are predicted for comparison to results shown in Fig. 20. Figure B.5 shows a bar chart comparing the uplift pressures, $\Delta\bar{P}$, for the leading-edge in areas A^L, A^R, B^L, B^R, C^L and C^R. Inspection of Figure B.5 confirms that a fully-developed flow field will result in uplift pressure reductions that are up to 20%.

From these simulations, it is shown that a fully developed profile is predicted to have slightly lower pressures (i.e., pressures are no more than 20% lower) than those predicted using the current experimental setup. The decrease in uplift pressure within a fully developed profile is due to the increased boundary layer thickness and lower velocity near the shingle surface. For the current study, Figure B.4(b) and Figure B.6 show there exists a much steeper velocity gradient near the shingle surface when using the predicted experimental profile, resulting in an increase in the predicted velocity at the

measurement location to 69 m/s from 60 m/s for a fully developed velocity profile for a flat shingle geometry.

Table B.1 StereoDIC analysis parameters and stereo camera specifications

Case	**Turbulence Intensity, I**	**Viscosity Ratio, $\mu t/\mu$**
1	5 (Fluent Default)	10 (Fluent default)
2	5	20
3	10	10
4	10	20
5	20	10
6	20	20

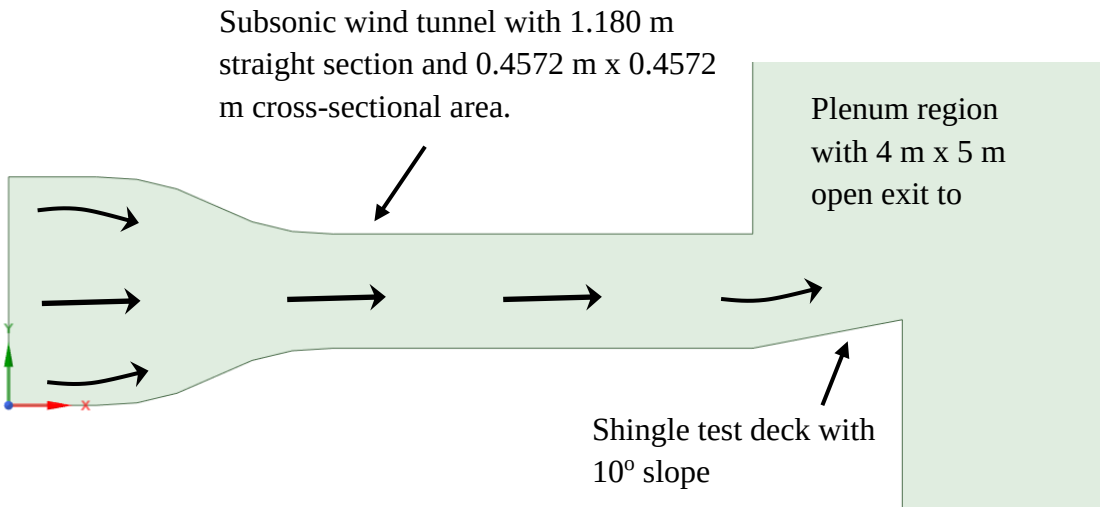

Figure B.1 2D domain schematic defined by the wind tunnel and shingle test deck.

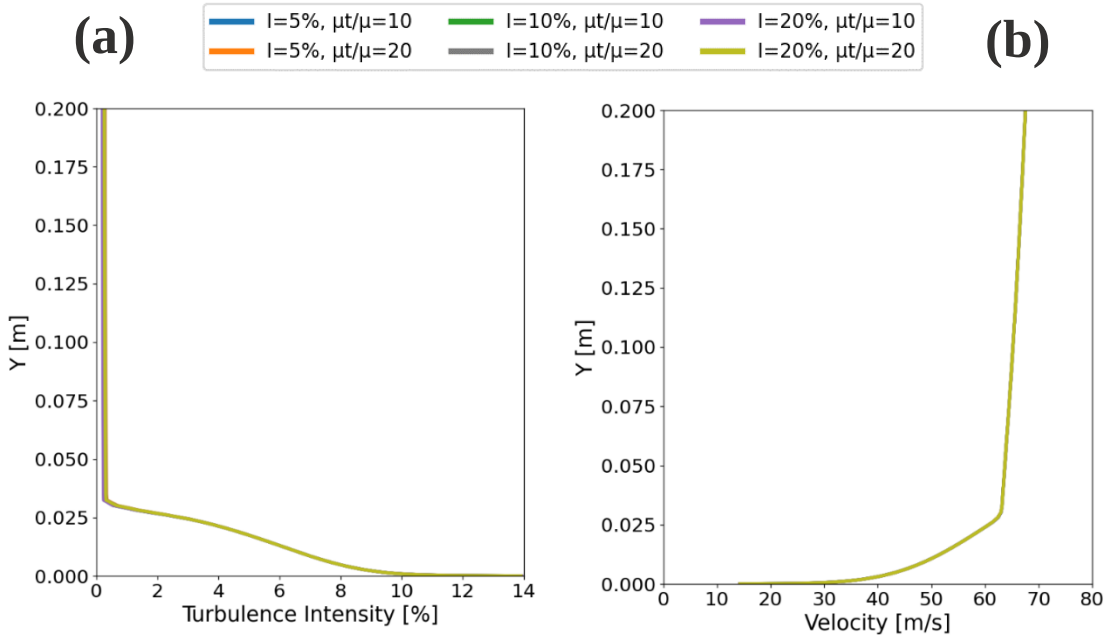

Figure B.2 (a) Turbulence intensity profile and (b) velocity profile near the exit of the wind tunnel for cases of varying inlet turbulence parameters

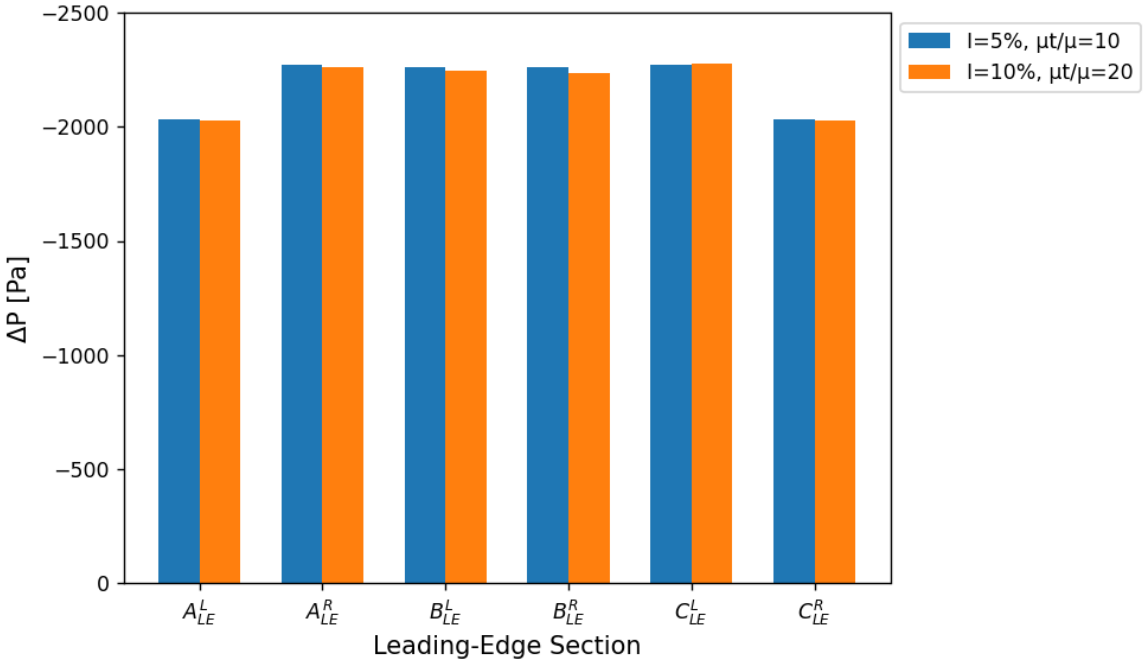

Figure B.3 Difference between pressure measurements at sections of the shingle's leading-edge when varying inlet turbulence parameters.

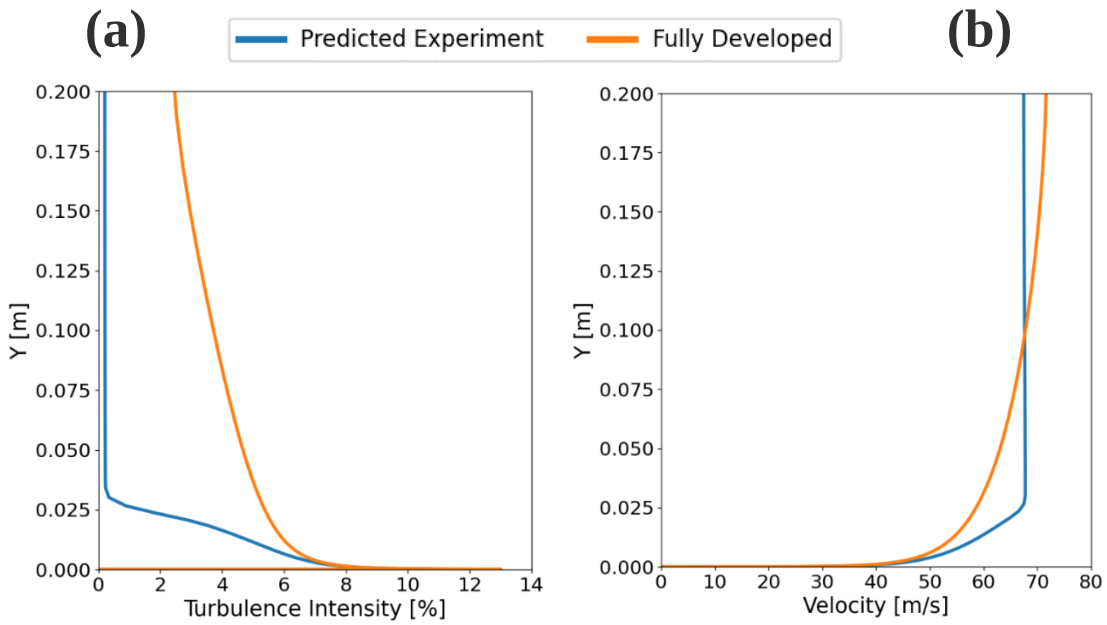

Figure B.4 Prescribed (a) turbulence intensity and (b) velocity profiles 590 mm away from the exit of the wind tunnel for the predicted experimental and fully developed boundary layers.

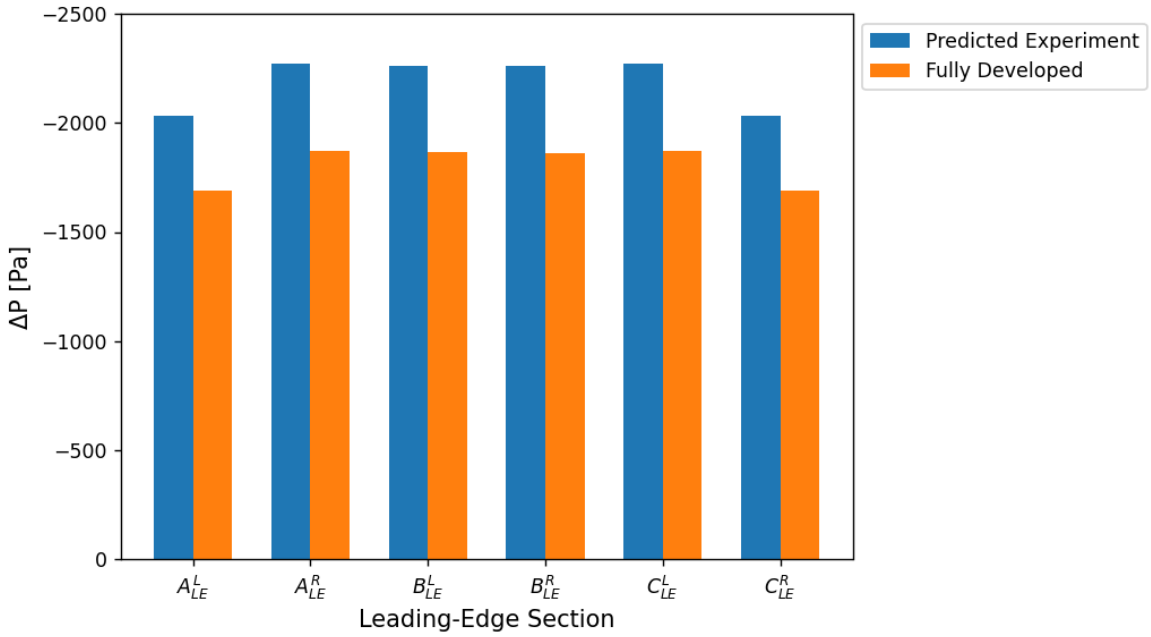

Figure B.5 Comparison of pressure measurements using velocity and turbulence intensity profiles of the experimental setup and a fully developed flow.

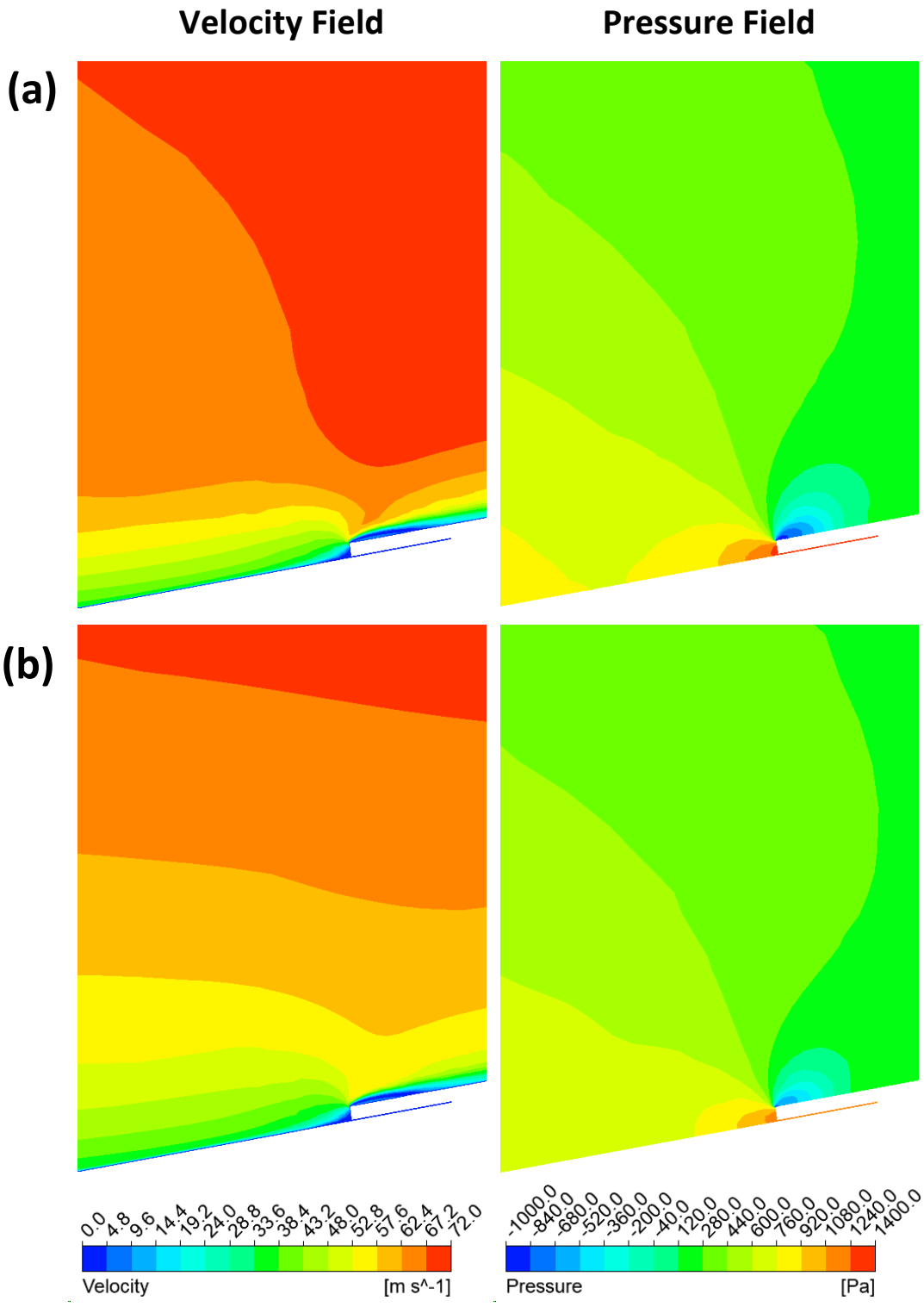

Figure B.6 Velocity magnitudes and pressure fields near the shingle for (a) predicted experiment velocity profile and (b) fully developed velocity profile.